Research paper

Phase Composition Maps integrate mineral compositions with rock textures from the micro-meter to the thin section scale

Kyle V. Willis [a], LeeAnn Srogi [a,*], Tim Lutz [a], Frederick C. Monson [b], Meagen Pollock [c]

[a] Department of Earth and Space Sciences, West Chester University of Pennsylvania, West Chester, PA 19383, USA
[b] Center for Microanalysis, Imaging, Research and Training, College of Arts and Sciences, West Chester University of Pennsylvania, West Chester, PA 19383, USA
[c] Department of Geology, College of Wooster, Wooster, OH 44691, USA

ABSTRACT

Textures and compositions are critical information for interpreting rock formation. Existing methods to integrate both types of information favor high-resolution images of mineral compositions over small areas or low-resolution images of larger areas for phase identification. The method in this paper produces images of individual phases in which textural and compositional details are resolved over three orders of magnitude, from tens of micrometers to tens of millimeters. To construct these images, called Phase Composition Maps (PCMs), we make use of the resolution in backscattered electron (BSE) images and calibrate the gray scale values with mineral analyses by energy-dispersive X-ray spectrometry (EDS). The resulting images show the area of a standard thin section (roughly 40 mm × 20 mm) with spatial resolution as good as 3.5 μm/pixel, or more than 81 000 pixels/mm^2, comparable to the resolution of X-ray element maps produced by wavelength-dispersive spectrometry (WDS). Procedures to create PCMs for mafic igneous rocks with multivariate linear regression models for minerals with solid solution (olivine, plagioclase feldspar, and pyroxenes) are presented and are applicable to other rock types. PCMs are processed using threshold functions based on the regression models to image specific composition ranges of minerals. PCMs are constructed using widely-available instrumentation: a scanning-electron microscope (SEM) with BSE and EDS X-ray detectors and standard image processing software such as ImageJ and Adobe Photoshop. Three brief applications illustrate the use of PCMs as petrologic tools: to reveal mineral composition patterns at multiple scales; to generate crystal size distributions for intracrystalline compositional zones and compare growth over time; and to image spatial distributions of minerals at different stages of magma crystallization by integrating textures and compositions with thermodynamic modeling.

1. Introduction

The formation of rocks and ore deposits is commonly inferred from microscale investigations of textures as well as rock and mineral compositions. Textures are investigated through measurements such as crystal size distributions (CSDs) and shape-preferred orientations obtained with a light microscope or by electron back-scatter diffraction (EBSD), or through numerical modeling (e.g., Higgins, 2006; Špillar and Dolejš, 2014; Rudge et al., 2008). X-ray computerized tomography (X-ray CT) provides a 3-dimensional spatial distribution of one or more mineral phases at the millimeter-to-centimeter scale (Ketcham and Carlson, 2001; Jerram et al., 2010). Rock and mineral compositions are separately investigated using a variety of methods. X-ray maps generated by wavelength-dispersive spectrometry (WDS) or energy-dispersive

spectrometry (EDS) are the standard technique for integrating compositional and textural information, and some studies have extended the technique. For example, Ginibre et al. (2002) combined WDS linescans produced by the electron probe microanalyzer (EPMA) with high-resolution back-scattered electron (BSE) images to characterize fine-scale oscillatory zoning within individual plagioclase phenocrysts. Humphreys (2009) used a similar approach to create images showing the progressive crystallization of plagioclase and the reduction of interstitial melt porosity in cumulate igneous rocks. These studies use high-resolution images of very small areas. Alternatively, phase identification and distribution is investigated through low-resolution X-ray mapping of larger sample areas by EPMA (Pret et al., 2010) or scanning X-ray analytical microscope (SXAM) using X-ray fluorescence (XRF) spectroscopy (Togami et al., 2000). None of these techniques is

---

* Corresponding author.
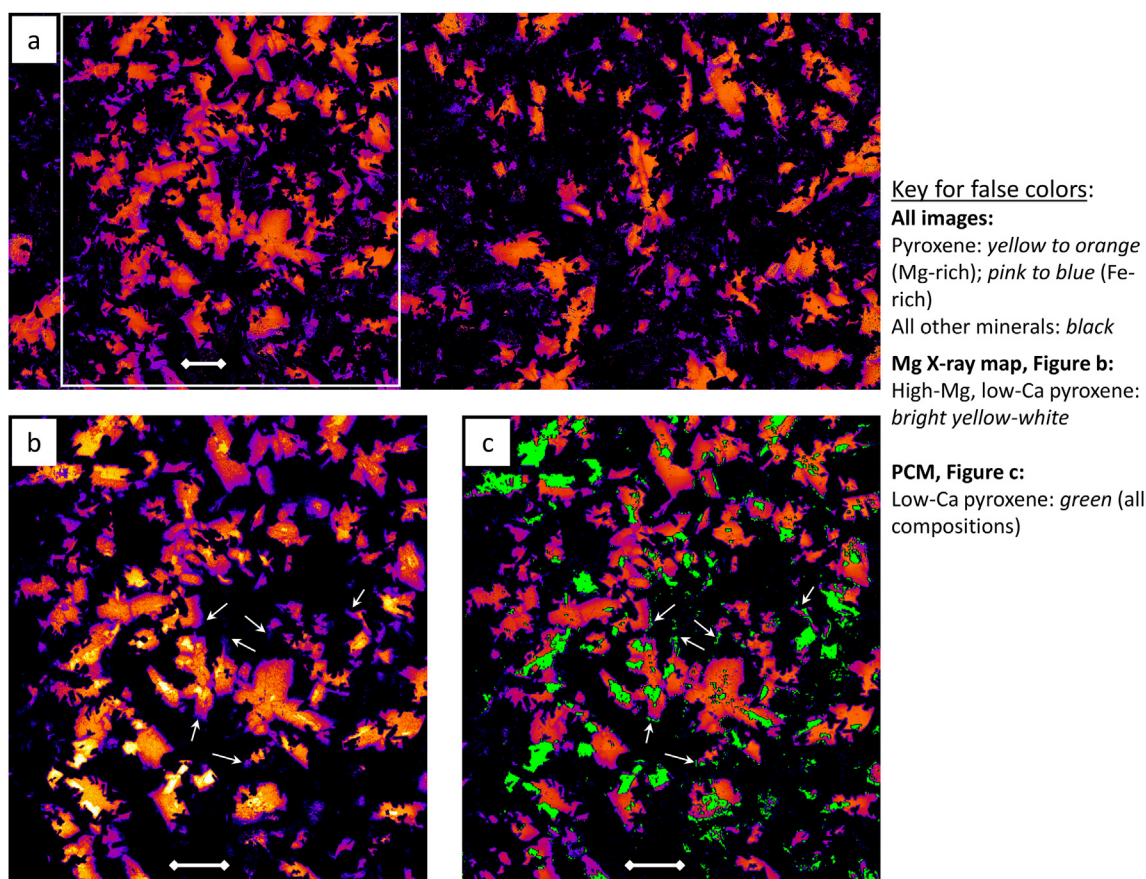 *E-mail address:* lsrogi@wcupa.edu (L. Srogi).

commonly used to produce high-resolution images of compositional variations within minerals over an area as large as a standard thin section (roughly 40 mm × 20 mm).

Recently, the QEMSCAN technology has made strides in automating the translation of EDS X-ray element maps into images of phase composition (Gottlieb et al., 2000). A typical QEMSCAN uses multiple silicon drift detectors to collect X-ray spectra simultaneously at high count rates resulting in rapid automated analysis with robust statistics. QEMSCAN is particularly effective for imaging ores and other samples that contain phases with large compositional contrasts. The QEMSCAN technique requires up to several hours of operator time before the run so that the algorithms correctly relate composition to phase identity, but a great time-saving advantage is automated image processing. At present, however, QEMSCAN is not widely-available and may be expensive for samples as large as a standard thin section. A high-resolution QEMSCAN of a standard thin section area, with analysis spacing of 5 μm or 40 000 spots/mm^2 and a dwell time of 0.010 s per spot, would require 320 000 s, or 89 h of run time.

This paper describes an alternative method using high resolution BSE images as the basis for creating maps of phase compositions or Phase Composition Maps (PCMs) of a standard thin section area, such as the example in Fig. 1a. We developed the PCM approach to overcome the limitations of X-ray element maps to produce images with good spatial resolution at a variety of area scales showing phases and compositions in texturally-heterogeneous, medium-grained rocks. EPMA or QEMSCAN X-ray element maps of whole thin sections were prohibitively expensive, and X-ray maps obtained with our SEM-EDS did not have sufficient

resolution. A BSE image with a 100 micro-second (μsec) dwell time takes 2–4 h to collect and montage and results in PCM images with a resolution as good as 3.5 μm/pixel or more than 81 000 pixels/mm^2. Utilizing the fact that gray scale value in a BSE image depends on the average atomic number of the material, gray scale values are calibrated for composition using EDS point analyses with 15–30 s analysis times and a detection limit of 0.1 wt.%. PCMs can be produced directly from the BSE image using threshold or similar functions in standard image processing software for minerals with simple compositions and no overlap of gray scale value. Multivariate linear regression is applied to minerals with solid solution, improving upon work by Ginibre et al. (2002) and Humphreys (2009) by using more robust regression models extended to more complex mineral solid solutions. Minerals in our samples with overlapping gray scale values require incorporation of up to three EDS X-ray element maps to produce PCMs for eight separate minerals. The complex samples described in this paper provide a *maximum* time estimate for PCM creation. In short, PCMs make the most of BSE imaging and EDS mineral analyses and X-ray maps using widely-available SEM-EDS instruments.

Fig. 1 shows that the resolution of mineral compositions in a PCM for a thin section (Fig. 1a and c) is comparable to a standard WDS X-ray map for a smaller area (Fig. 1b), and illustrates how the phase map can be better than the elemental X-ray map (see Appendix for sample and analysis details). The X-ray map shows Mg-rich low-Ca pyroxene clearly (bright yellow-white in Fig. 1b), but other pyroxene compositions have overlapping Mg concentrations which therefore cannot be distinguished by false colors, and Fe-rich pyroxene barely shows up in the image. X-ray maps require further image processing of elemental concentrations to

Key for false colors:
All images:
Pyroxene: *yellow to orange* (Mg-rich); *pink to blue* (Fe-rich)
All other minerals: *black*

Mg X-ray map, Figure b:
High-Mg, low-Ca pyroxene: *bright yellow-white*

PCM, Figure c:
Low-Ca pyroxene: *green* (all compositions)

Fig. 1. Phase composition maps (PCMs) compared with elemental WDS X-ray map of sample DQ-6, a mafic igneous rock; see Appendix for sample and analytical details. All images were made using the same false colors (Fire Lookup Table in ImageJ). Scale bars are about 1 mm. White arrows point to grains of Fe-rich, low-Ca pyroxene that are virtually invisible or could be mistaken for augite rims in the element map (Fig. 1b) but are clearly visible as green grains on the PCM (Fig. 1c); see text for discussion. a) Pyroxene PCM; high-Ca pyroxene (augite) and low-Ca pyroxene are not separated. Thin section area is 41.72 mm × 18.03 mm and contains 11 552 pixels × 4992 pixels, for a spatial resolution of about 3.6 μm/pixel or 76 664 pixels/mm^2. White outlined box is the area shown in Fig. 1b and c. b) EPMA-WDS X-ray map for Mg. Augite and low-Ca pyroxene are not separated except that Mg-rich, low-Ca pyroxene is bright yellow-white. c) Cropped and enlarged portion of the pyroxene PCM (same area as the Mg X-ray map), with the low-Ca pyroxene PCM as an overlay in green (false color applied in ImageJ).
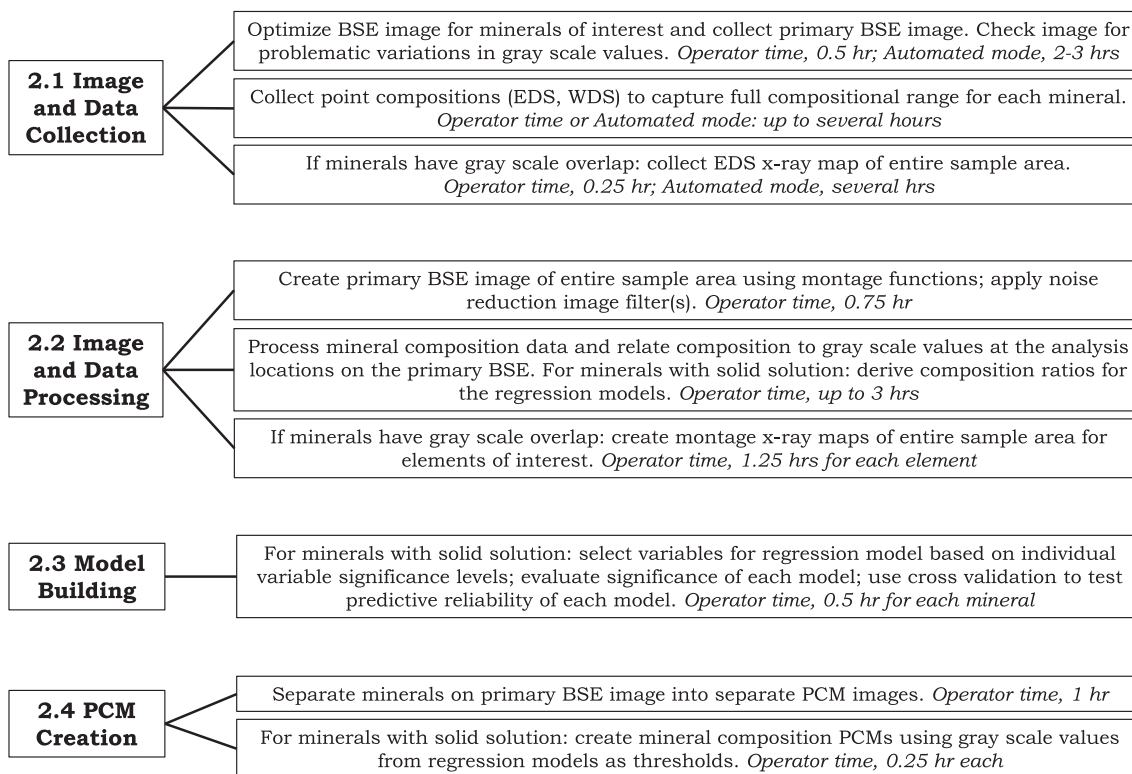
2.1 Image and Data Collection	Optimize BSE image for minerals of interest and collect primary BSE image. Check image for problematic variations in gray scale values. *Operator time, 0.5 hr; Automated mode, 2-3 hrs*
	Collect point compositions (EDS, WDS) to capture full compositional range for each mineral. *Operator time or Automated mode: up to several hours*
	If minerals have gray scale overlap: collect EDS x-ray map of entire sample area. *Operator time, 0.25 hr; Automated mode, several hrs*

2.2 Image and Data Processing	Create primary BSE image of entire sample area using montage functions; apply noise reduction image filter(s). *Operator time, 0.75 hr*
	Process mineral composition data and relate composition to gray scale values at the analysis locations on the primary BSE. For minerals with solid solution: derive composition ratios for the regression models. *Operator time, up to 3 hrs*
	If minerals have gray scale overlap: create montage x-ray maps of entire sample area for elements of interest. *Operator time, 1.25 hrs for each element*

| 2.3 Model Building | For minerals with solid solution: select variables for regression model based on individual variable significance levels; evaluate significance of each model; use cross validation to test predictive reliability of each model. *Operator time, 0.5 hr for each mineral* |

| 2.4 PCM Creation | Separate minerals on primary BSE image into separate PCM images. *Operator time, 1 hr* |
| | For minerals with solid solution: create mineral composition PCMs using gray scale values from regression models as thresholds. *Operator time, 0.25 hr each* |

Fig. 2. Chart outlining the major steps to create PCMs with our approximate timing based on our instruments and software. Numbers refer to sections in the text and Appendix.

show mineral phases. Phase maps, such as the PCMs in Fig. 1c, clearly show separate grains of high-Ca and low-Ca pyroxene including the Fe-rich rims, resolving the ambiguity in the X-ray map (compare grains highlighted by the white arrows in Fig. 1b and c).

In the Results section below, three applications show the versatility of

PCMs as a petrologic tool to:

1) image centimeter-scale spatial patterns of mineral composition variation over larger areas than traditional X-ray maps while preserving compositional details a few micro-meters in dimension;
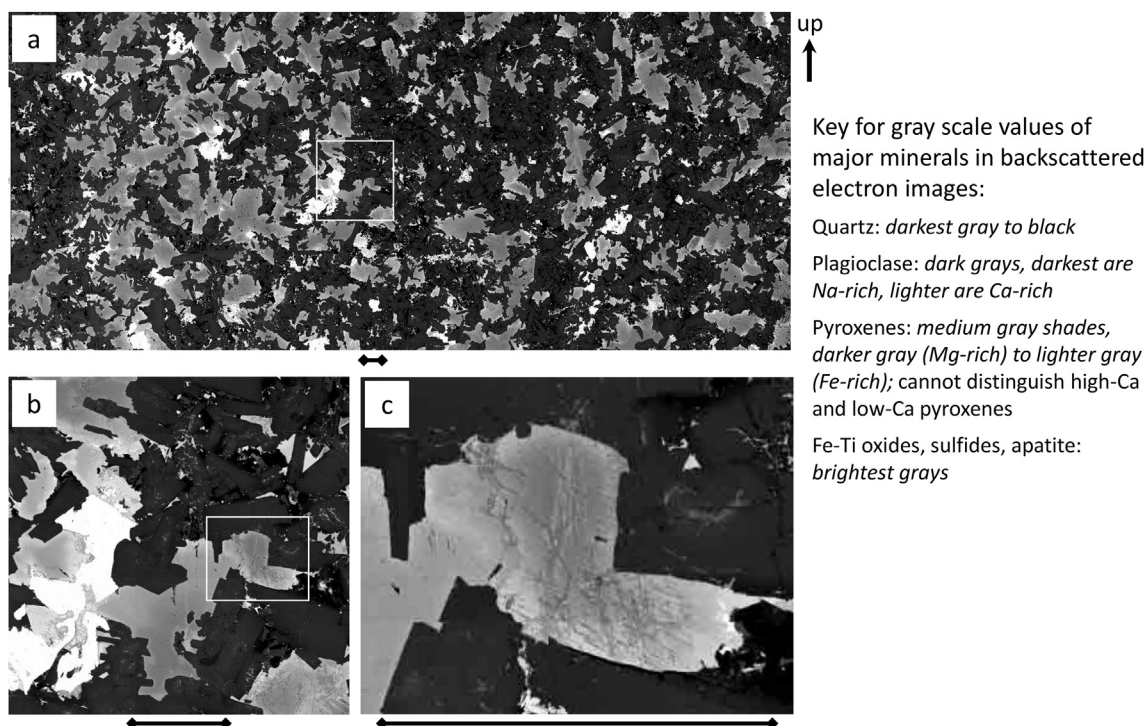

up

Key for gray scale values of major minerals in backscattered electron images:

Quartz: *darkest gray to black*

Plagioclase: *dark grays, darkest are Na-rich, lighter are Ca-rich*

Pyroxenes: *medium gray shades, darker gray (Mg-rich) to lighter gray (Fe-rich); cannot distinguish high-Ca and low-Ca pyroxenes*

Fe-Ti oxides, sulfides, apatite: *brightest grays*

Fig. 3. Primary BSE image of sample DQ-6. Scale bars are about 1 mm a) Area of thin section and pixel resolution are the same as in Fig. 1a. White outline is area of Fig. 3b. b) Cropped and enlarged portion of Fig. 3a. White outline is area of Fig. 3c. c) Cropped and enlarged portion of Fig. 3b. See text for discussion.
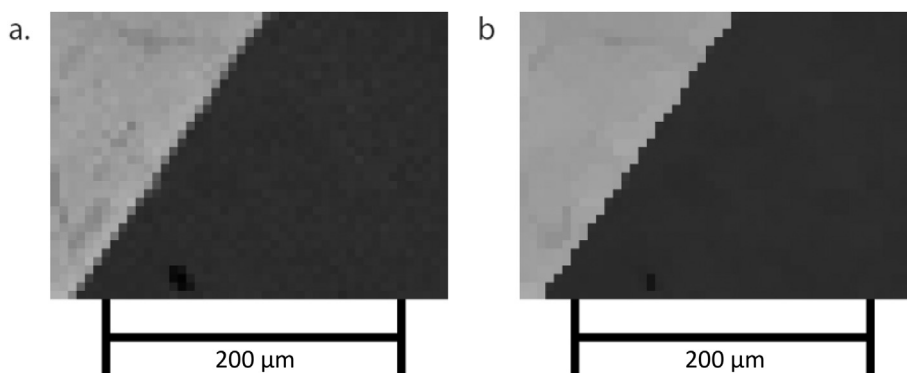
Fig. 4. Comparison of the same BSE image a) prior to the application of the facet pixilation filter and b) after application of the facet filter. See text for discussion.

2) provide images of intracrystalline zoning for measuring crystal size distributions and comparing rates and processes of crystal growth;
3) create images of co-crystallizing minerals and interstitial liquid derived from thermodynamic models of phase equilibria thus integrating spatial distributions with mineral compositions at the thin section scale.

Similar applications could be made for diagenetic sequences in sedimentary rocks, inclusion-poikiloblast-fabric relationships in metamorphic rocks, or the paragenesis of ore deposits.

2. Methods

The samples discussed in this paper are mafic igneous rocks, specifically tholeiitic diabase (also called dolerite) from the western Newark rift basin, Pennsylvania, U.S.A. The Newark basin is part of the Central Atlantic Magmatic Province (CAMP), a large igneous province formed about 201 Ma during rifting of Pangaea and opening of the Atlantic Ocean (Hames et al., 2003; Marzoli et al., 2011; Withjack et al., 2012). In the western Newark basin, post-magmatic tilting and folding has exposed an upper-crustal cross section from the Jacksonwald basalt at the Jurassic

paleo-surface to about 5–6 km depth (Srogi et al., 2010; Martinson et al., 2015). The Jacksonwald basalt and the underlying plutonic rocks are correlative with the Orange Mtn. basalt and the Palisades Sill, respectively, in the eastern Newark basin, New Jersey (Marzoli et al., 2011). Samples DQ-6 and DQ-136 were collected from the 255-m wide Birdsboro Dike in the Dyer Quarry, Birdsboro, PA. Samples from basal portions of two sills were collected from the Pennsylvania Granite Quarry,

Table 1
Variable lists for pyroxene model for sample EQ-169.

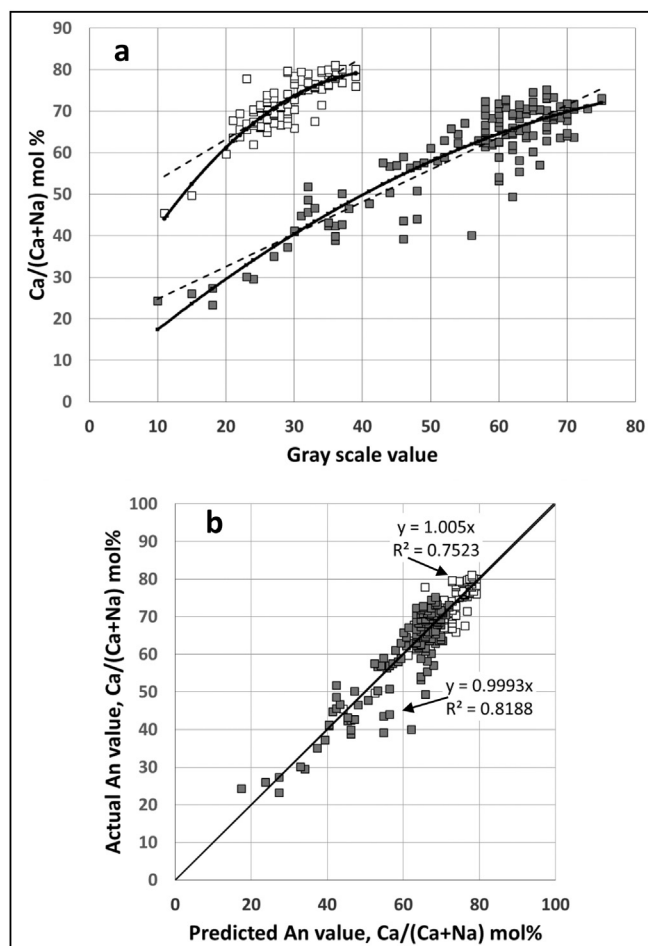| Variable Name	Collection procedure
Base Terms	
Gray Scale	Collected using eye drop tool in Photoshop
Mg Con	Collected by EDS and calculated as the mole % of Mg divided by the mole % of (Mg + Fe + Ca)
Fe Con	Collected by EDS and calculated as the mole % of iron divided by the mole % of (Mg + Fe + Ca)
High Ca	Indicator variable set to 1 if the Ca concentration is higher than 0.25 and 0 if less than 0.25
Squared Terms	
Gray Scale squared	Calculated by squaring the Gray Scale value
Mg Con squared	Calculated by squaring the magnesium concentration
Fe Con squared	Calculated by squaring the iron concentration
Interaction Terms	
Gray Scale * Mg Con	Calculated by multiplying the Gray Scale value by the magnesium concentration
Gray Scale * Fe Con	Calculated by multiplying the Gray Scale value by the iron concentration
High Ca * Mg Con	Calculated by multiplying the high calcium indicator by the magnesium concentration
High Ca * Fe Con	Calculated by multiplying the high calcium indicator by the iron concentration
Selected Variables	Variable p-values for regression to predict gray scale value from composition
Mg Con	0.0013
Fe Con	0.0161
High Ca	0.0045
Mg Con squared	0.0005
High Ca * Mg Con	0.0025

Fig. 5. Results of multivariate linear regression models for plagioclase in sample EQ-169 (squares with white fill) and sample DQ-136 (squares with gray fill). a) Molar Ca proportion (or An value) in mol % vs. gray scale value. Solid lines: relationship from regression (see text for equations). Dashed lines: linear trendlines through the data points from Excel. The better fit of the regression should be noted. b) Actual An value vs. An value predicted by the multivariate regressions. The equations are best-fit trendlines for each sample from Excel, forced through the origin and show how closely the data approach a 1:1 correlation.

Elverson quadrangle, PA, (EQ-169) and the Douglassville Traprock Quarry, Boyertown quadrangle, PA, (BoQ-3). Both sill samples contain accumulated phenocrysts of Mg-rich orthopyroxene and sample BoQ-3 contains a little olivine.

Methods to produce PCMs for samples DQ-6, DQ-136, EQ-169, and BoQ-3 are outlined in Fig. 2 and described below. All samples were polished thin sections, 30 μm thick, of standard size measuring 21 mm × 40 mm or 27 mm × 46 mm. Images were cropped to the largest rectangle entirely within the rock on the thin section, resulting in somewhat smaller dimensions. Operator time estimates in Fig. 2 are *maxima* for PCM creation because our samples contained two or three mineral species of variable composition with overlapping gray scale values and some processing steps were run on an old computer with Windows XP operating system. Operating conditions specific to the instruments we used are provided in the Appendix section 2.

2.1. Image and data collection

2.1.1. Image collection

To create the PCM a high-resolution BSE image is acquired, referred to as the primary BSE image; an example is shown in Fig. 3 (operating conditions are in Appendix section 2.1.1). Distinguishing phase and composition variations in a BSE image requires that each mineral have

Fig. 6. Results of multivariate linear regression models relating gray scale value to Mg proportion (mol %) for high-Ca pyroxene (circles with light gray fill) and low-Ca pyroxene (circles with dark gray fill). A single regression equation fit to all pyroxene compositions in each sample is shown by the solid line and stated in the text. a) sample EQ-169. b) sample DQ-136. Inset charts show the correlation of actual Mg proportion with that predicted by the multivariate regressions. The equations are best-fit trendlines from Excel forced through the origin and show how closely the data approach a 1:1 correlation.

the largest unique range of gray scale values possible; we refer to this as "optimizing" the gray scale BSE image. This is achieved by adjusting the appropriate microscope controls to alter the production of backscattered electrons from each mineral. We optimize the gray scale range for all minerals of interest (plagioclase and pyroxenes in our samples) before capturing the primary BSE image. Gray scale values of the primary BSE image were not adjusted during later image processing to avoid introducing bias or error into the relationship between gray scale and composition.

To relate gray scale value to composition with accuracy, it is critical that gray scale value for the same phase with the same composition be as uniform as possible, within a few values, across the sample area. Systematic shifts in gray scale that are not due to phase composition can result from non-uniform thickness of the carbon coating or variations in running conditions during image capture, such as drift in voltage or beam current. After BSE image acquisition is complete we check the quality of the BSE image before further processing (Appendix section 2.1.1).

2.1.2. Composition data collection

Point analyses of mineral compositions obtained by EDS or WDS are used to calibrate the gray scale values in the primary BSE image. Mineral analysis was the single largest proportion of operator time for our procedure (Fig. 2), but may not be much additional time since it is already a routine part of rock characterization. Automated analysis of pre-set locations would reduce operator time significantly. Analyses should be taken from across the sample area to account for normal variability in gray scale values. For minerals with solid solution, it is important to take enough analyses to span the range of compositions present but the number of points needed depends on the range and complexity of the solid solution. In order to test the reliability of the linear regression models, enough composition points for each mineral should be collected so that a random subset (25%) can be extracted (the holdout dataset) while the remainder is used to build the regression models (see section 2.3 below). We collected approximately 120 point compositions for plagioclase feldspar, 150 for pyroxene, and 80 for olivine by EDS (operating conditions in Appendix section 2.1.2). We verified our EDS mineral compositions by analyzing the same samples and grains using EPMA-WDS at the University of Massachusetts-Amherst (operating conditions in Appendix section 1).

2.1.3. X-ray element map collection

We collect X-ray maps of indicator elements when gray scale values are not enough to uniquely distinguish minerals in the images. The X-ray element maps only need to be of a high enough quality to show relative concentrations of indicator elements; they do not have the information depth or spatial resolution of small-area WDS X-ray maps or of the primary BSE image. It is critical that the thin section not be removed from the sample chamber between collection of the primary BSE image and the X-ray maps so that all images can be aligned properly. When X-ray maps are acquired, a new BSE image also is acquired to facilitate accurate alignment with the primary BSE image; we call this the alignment BSE image. Operating conditions for EDS X-ray maps are in Appendix section 2.1.3.
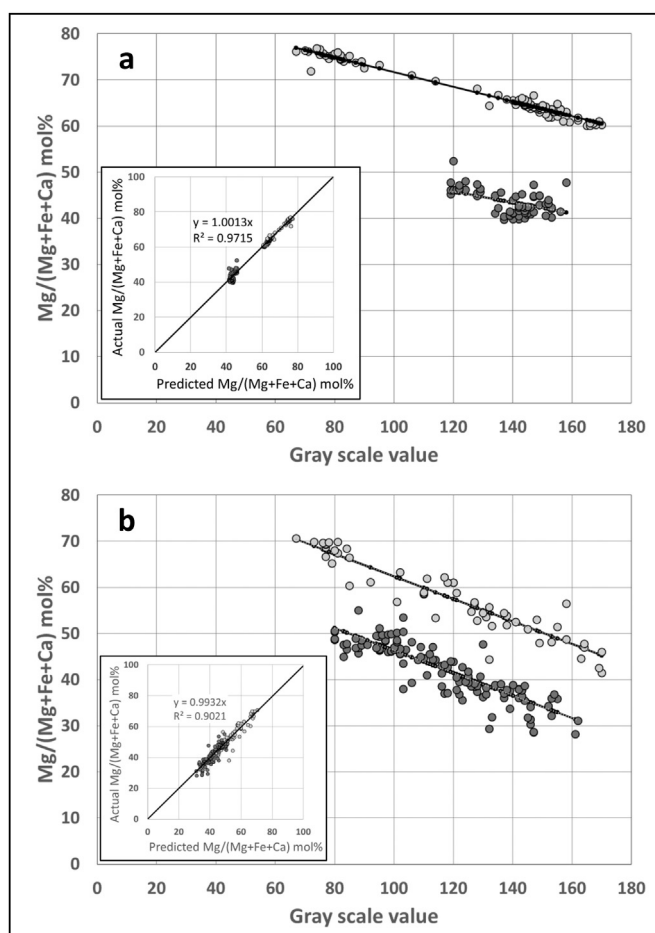
Table 2
Model significance terms.

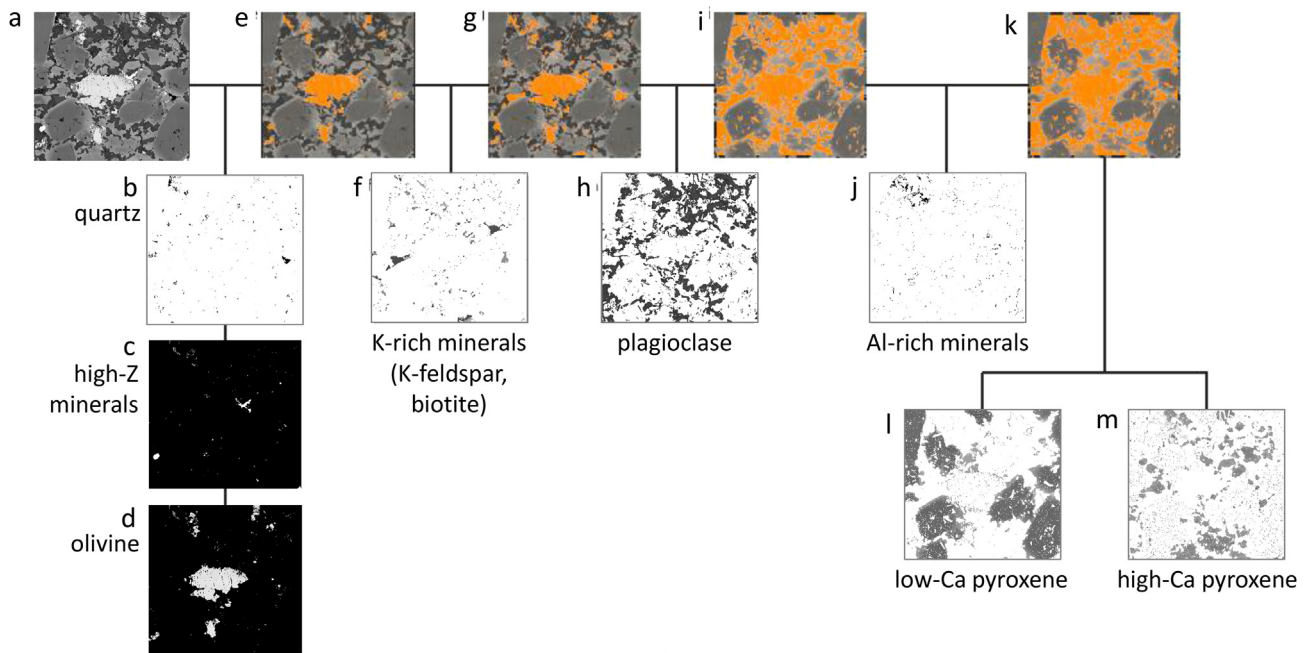| Mineral	F-test	R^2 value	Shrinkage
Sample EQ-169			
Plagioclase	<0.0001	0.969	0.01
Pyroxene	<0.0001	0.7075	−0.17
Sample DQ-136			
Plagioclase	<0.0001	0.8146	0.004
Pyroxene	<0.0001	0.9146	0.001

Fig. 7. Flow chart illustrating the mineral separation process. Orange pixels are those removed from the primary BSE image. a) portion of the primary BSE image for sample BoQ-3 before any phase removal; resolution is about 3.5 μm/pixel or 81 394 pixels/mm^2. Step 1: b) image of quartz (lowest gray scale values); c) image of oxides and other high- Z minerals; d) image of olivine. Background in Fig. 8c and d is made black to reveal pixels that have high gray scale values close to white. e) processed image with orange pixels replacing the removed pixels of quartz, oxides, and olivine. Step 2: f) image of potassium-rich minerals; g) processed image after removing K-rich minerals. Step 3: h) image of plagioclase; i) processed image after removing plagioclase. Step 4: j) image of aluminum-rich minerals; k) processed image after removing Al-rich minerals. Step 5: l) image of low-Ca pyroxene; m) image of high-Ca pyroxene. (For interpretation of the references to colour in this figure legend, the reader is referred to the web version of this article.)

2.2. Image and data processing

2.2.1. Create the BSE image montage of the entire sample area and remove image artifacts

Images were processed using the proprietary Oxford Inca software and Adobe Photoshop (Appendix 2.2.1) but these tasks can be completed with other SEM-EDS and image processing software. To obtain a high-resolution BSE image such as Fig. 3, the sample area is divided into smaller areas (frames) and an image of each is captured with a resolution of 1024 × 1024 pixels. The frames are then stitched together with image processing software to create a montage image that preserves as much resolution as possible. For example, in generating the primary BSE image, a rectangular thin section area measuring 40 mm × 20 mm is divided into 24 frames × 12 frames with a 25-pixel overlap between frames. Each frame measures a little less than 1.67 mm × 1.67 mm, contains about 1.05 million pixels, and has a resolution of about 0.00163 mm/pixel or 1.63 μm/pixel. In principle, the 288 frames could be stitched together

and maintain the high resolution of 1.63 μm/pixel; in practice, however, these images are too large to handle and impossible for the operator to stitch accurately. The critical step is using the proprietary Inca software to automatically stitch a few frames to create larger areas ("tiles") with 1024 × 1024 resolution, and then put these tiles together in Adobe Photoshop to achieve resolution ranging from about 2.4 to 6.5 μm/pixel in the final montage (Appendix 2.2.1). The primary BSE in Fig. 3a shows the thin section area of 41.72 mm × 18.03 mm, which contains 11 552 pixels × 4992 pixels and has a spatial resolution of about 3.6 μm/pixel or 76 664 pixels/mm^2; the TIFF file of this image is about 654 Mb). The effective resolution of this primary BSE image is indicated by increasing the magnification of the images or "zooming in" (Fig. 3b and c). For comparison, a montage of the same thin section area with 2048 × 1024 pixels has resolution of about 20 μm/pixel; we consider this a low-resolution image. Pixel resolutions are noted in the Figures and provided in Appendix section 2.2.1.

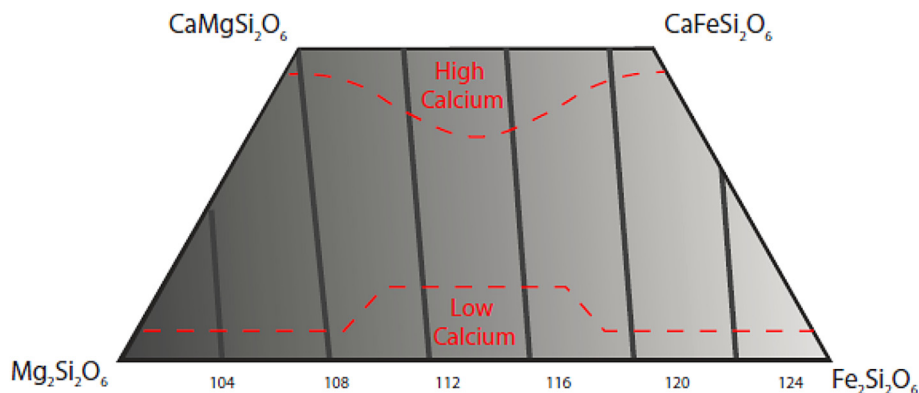Compositional artifacts are introduced when the boundary between

Fig. 8. The pyroxene quadrilateral showing common compositions (dashed lines). Solid lines: contours of average atomic number. Gradational background shading represents changing gray scale values with composition. Both high- and low-Ca pyroxenes can have the same average atomic number and the same gray scale value due to the three-component solid solution in Mg, Fe, and Ca.

Table 3
Mineral proportions in DQ-136 thin section.

Mode			Phase Composition Map	
Mineral	counts	area %	Mineral	area %
Plagioclase[a]	420	41	Plagioclase	43
Pyroxenes[b]	425	41	High-Ca Pyroxene	23
			Low-Ca Pyroxene	16
Hornblende	28	3	Al-rich minerals[e]	4
Quartz	37	4	Quartz	3
K-feldspar	28	3	K-rich minerals[f]	10
Granophyre[c]	11	1		
Biotite	41	4		
Opaque + Accessory[d]	42	4	High-Z minerals[d]	2
Total	1032	100	Total	101

Notes

Mode: standard point count on a grid using a mechanical stage and a Leica DMR-XP polarizing light microscope.

PCM: pixel areas for each mineral measured using the threshold function in ImageJ.

[a] Includes a few percent sericitized plagioclase.

[b] High-Ca and low-Ca pyroxenes not separately counted.

[c] Too fine-grained to count quartz and K-feldspar separately.

[d] Ulvöspinel (magnetite), ilmenite, some sulfides; accessory minerals are mostly apatite.

[e] Mostly hornblende and secondary alteration minerals.

[f] K-feldspar, very fine-grained granophyre, and biotite.

adjacent minerals falls within a single pixel because the resultant gray scale value is a weighted average of the gray scale value of each mineral in the pixel (Fig. 4a). Such artifacts can lead to incorrect phase identification and can introduce errors into estimated mineral modes or compositions. We used Photoshop's facet pixelation filter to correct this problem (Fig. 4b). This image filter applies an algorithm to re-assign gray scale values of each pixel along the boundary in place of the weighted average value; the details of the procedure and the algorithm are part of the Photoshop proprietary software. The presence of micro-scale cracks, inclusions and other features means that compositional artifacts can be reduced but not eliminated entirely.

2.2.2. Correlate gray scale values with compositions

A gray scale value in the primary BSE image is determined at the location of each composition point analyzed on minerals with solid solution. The gray scale values observed at the time of point analysis are not necessarily the same as in the primary BSE image. We visually identified each composition point on the primary BSE image and used the eye drop tool in Photoshop to obtain the gray scale value. If the area of the analysis is significantly larger than the area of a single pixel, then the gray scale values should be averaged over that area. Having x-y coordinates of each analysis point makes finding the locations easier, and could be made faster if the SEM-EDS software stores the x-y coordinates as part of the BSE image.

2.2.3. Create X-ray map montages of the entire sample area

This step is only needed for samples containing phases with overlapping gray scale values. We followed the same procedure to produce the montage X-ray maps as for the primary BSE image, as described in Appendix section 2.2.3.
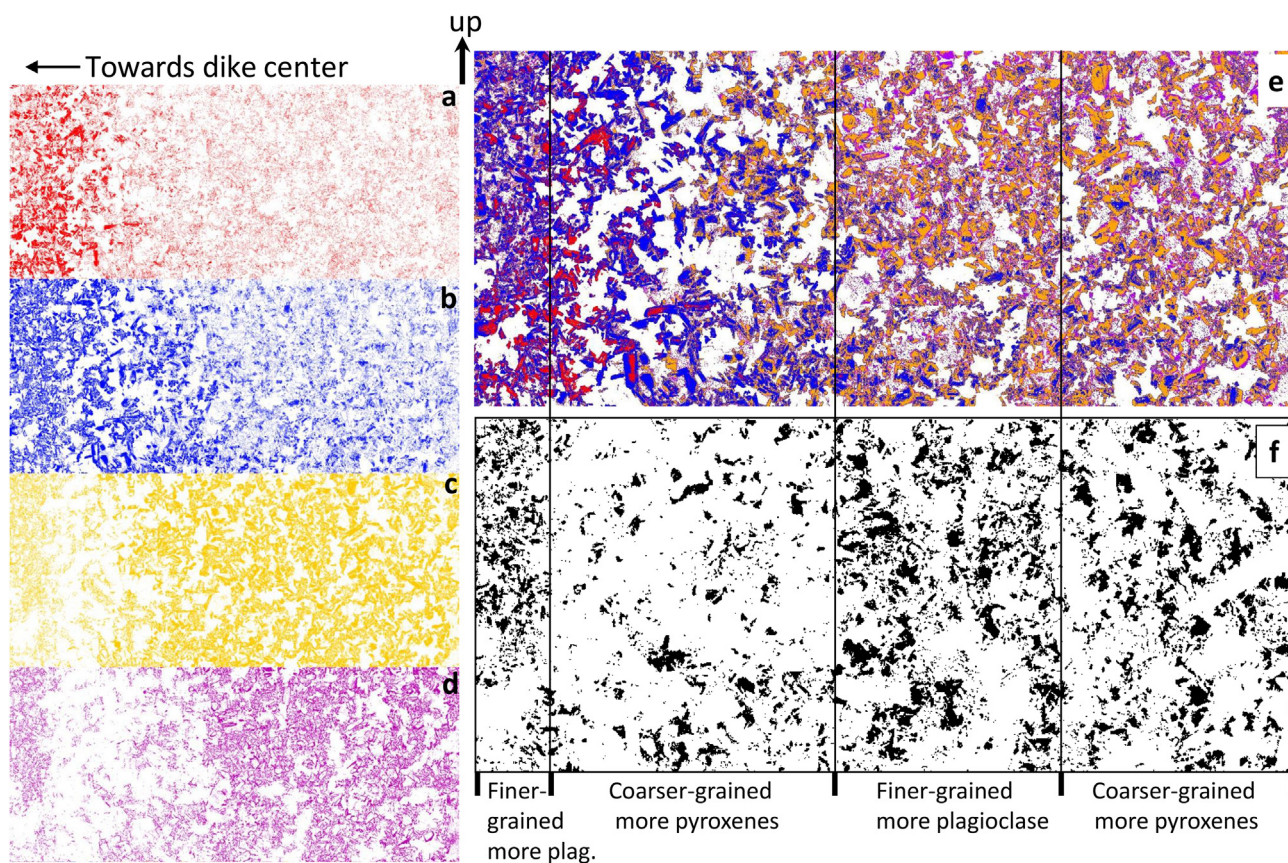
Fig. 9. PCMs for sample DQ-6 with the same area and pixel resolution as in Fig. 1a and 3a (see Appendix 3.1 for image details). Each image shows the thin section in its original orientation (note up arrow). Boundaries of layers with different grain sizes and proportions of plagioclase and pyroxene are shown on 9f and 9e. a-e) PCMs showing plagioclase color-coded by composition: (An$_{60-50}$: *red*; An$_{49-40}$: *blue*; An$_{39-30}$: *yellow*; An$_{29-20}$: *purple*; all other minerals: *white*). Fig. 9a–d shows individual composition ranges; Fig. 9e shows all plagioclase compositions combined. The systematic change in the abundance of different plagioclase compositions should be noted. The appearance of "speckling" is due to small plagioclase grains included within pyroxenes or intergrown with quartz in interstitial areas. f) PCM showing late-stage phases (black pixels): quartz, K-feldspar, biotite, and a small amount of secondary muscovite (sericite). Variation in the abundance and distribution of late-stage minerals across the thin section should be noted. See text for discussion.
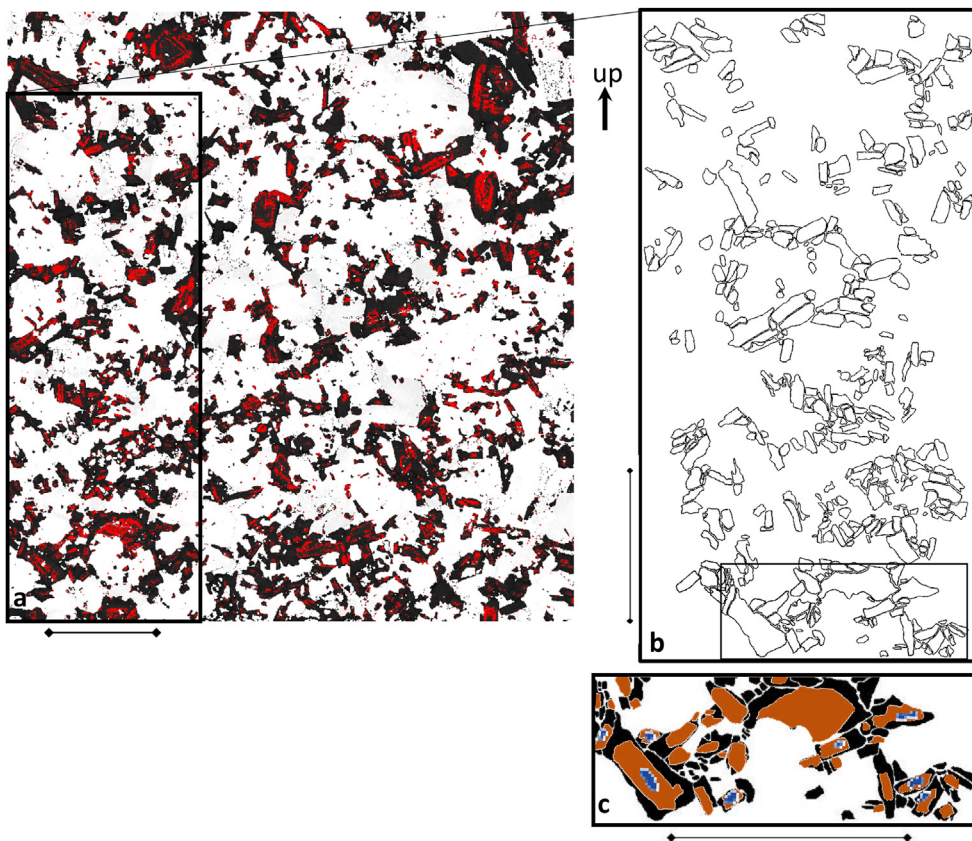
Fig. 10. Plagioclase in EQ-169. Scale bars are 2 mm a) Part of the PCM; spatial resolution is about 5.4 μm/pixel or 34 229 pixels/mm2. Red pixels: calcic shell, An_{81-76}; black pixels: cores and outer shells, An_{76-44}. Black rectangle is the area of Fig. 10b. b) Outlines of outer shells (entire grains) used in CSD. Black rectangle is area of Fig. 10c. c) Enlarged composite showing filled outlines of cores (blue), calcic shells (orange), outer shells (black).
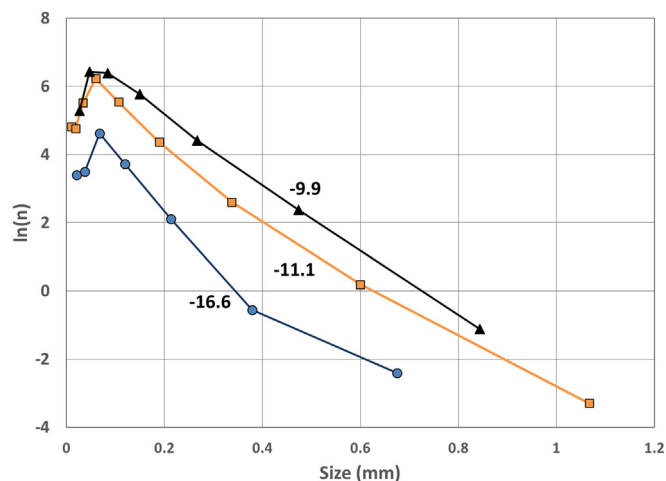

Fig. 11. CSDs for different compositional portions of plagioclase in sample EQ-169. Blue circles and line: cores with composition An_{75-60}; N = 237. Orange squares and line: calcic shells with composition An_{81-76}; N = 703. Black triangles and line: entire grains including sodic outer shells with composition An_{76-44}; N = 464. Numbers are slopes for the dashed lines which best fit all or part of the data. (For interpretation of the references to colour in this figure legend, the reader is referred to the web version of this article.)

2.3. Building the multivariate linear regression models

The ability to associate gray scale with composition for minerals with solid solution greatly increases the quantitative value of a BSE image. Multivariate linear regression is used to model the numerical relationship between gray scale value and composition. Multivariate linear regression

is more robust than "straight-line fitting" because it incorporates more variables including interaction parameters between variables, and can account for non-linear relationships. Statistical software makes regression modeling relatively easy and rapid; we used the Statistical Analysis Suite commercial software (SAS Product Documentation version 9.4) for which our U.S. University has a site license. The general approach is summarized below; details pertaining to SAS are in Appendix section 2.3.

2.3.1. Solid solution and selection of variables

In our samples, solid solution exists in olivine, plagioclase, and pyroxenes. Table 1 shows an example input list of variables for the pyroxene model for sample EQ-169 and how the data were collected or calculated. The last section of Table 1 shows the variables selected as significant by a stepwise procedure in the statistical modeling software and the corresponding p-values for the prediction of gray scale value from composition. The p-value is the probability that a variable identified as significant is not significant; lower p-values are better. For each mineral three regression equations are produced to predict gray scale and two composition parameters. The main composition equations are stated below and more details are in Appendix section 2.3.1.

Olivine composition is binary, expressed as the molar proportion of [Mg/(Mg + Fe)], also called Forsterite (Fo) value. Olivine in sample BoQ-3 has a linear relationship between gray scale value (GS) and composition:

$$\text{Fo value (mol. \%)} = 0.92888 + (-0.00141 \times \text{GS}) \tag{1}$$

For plagioclase, example regression equations derived from the multivariate analysis to predict An value from gray scale value are:

For sample EQ-169:

$$\text{Ca (mol. \%)} = 0.15825 + (0.02954 \times \text{GS}) - (0.00034 \times \text{GS}^2) \tag{2}$$

Table 4
Geochemical composition of sample DQ-136 compared with lava flows and chill margins, western Newark basin.

Major elements (weight %)			Trace elements (ppm)			REE (ppm, not normalized)		
Oxide[a]	DQ-136	Flows & chills ave. ± st. dev.	Elem.	DQ-136	Flows & chills range	Elem.	DQ-136	Flows & chills range
SiO_2	53.03	52.97 ± 0.49	Sc	33.9	30.7–37.2	La	45.02	40.06–44.36
TiO_2	1.16	1.15 ± 0.04	V	252.5	235.9–272.6	Ce	38.56	35.00–37.44
Al_2O_3	13.53	14.14 ± 0.25	Cr	313.7	246.8–365.3	Pr	33.87	30.74–32.99
$Fe_2O_3^*$	11.43	11.10 ± 0.21	Ni	108.9	72.0–89.3	Nd	29.10	27.29–29.06
MnO	0.17	0.18 ± 0.01	Cu	108.4	96.3–113.0	Sm	22.89	21.67–22.80
MgO	7.99	7.52 ± 0.28	Rb	24.8	7.3–26.1	Eu	19.65	18.70–19.48
CaO	9.95	10.11 ± 1.15	Sr	169.4	168.5–226.9	Tb	17.94	17.24–18.04
Na_2O	2.10	2.47 ± 0.91	Y	22.3	21.2–23.5	Gd	19.58	18.05–19.44
K_2O	1.07	0.62 ± 0.24	Zr	91.7	93.1–101.2	Dy	16.25	15.15–16.28
P_2O_5	0.15	0.15 ± 0.01	Nb	7.9	7.2–7.8	Ho	15.20	13.99–15.20
Total	100.59	100.40 ± 0.55	Ba	175.4	131.4–174.8	Er	14.25	13.36–14.36
						Yb	12.69	11.82–12.69
						Lu	12.64	12.45–13.22

[a] $Fe_2O_3^*$ is total iron measured as Fe_2O_3. See Appendix section 3.3 for chemical analysis methods.

For sample DQ-136:

$$Ca \ (mol. \ \%) = 0.03824 + (0.01426 \times GS) - (0.000069 \times GS^2) \quad (3)$$

Most previous workers have approximated the relationship between composition and gray scale value in plagioclase as a straight line, but Fig. 5a and b show that our data are non-linear and that our regression model equations fit better than linear trendlines.

Pyroxene compositions are expressed as the molar proportion of [Mg/ (Mg + Fe + Ca)] or Mg Con (Table 1). In our samples, there are two pyroxene phases in abundance: high-Ca pyroxene or augite, with molar proportion of [Ca/(Mg + Fe + Ca)] more than 0.25; and a low-Ca pyroxene with Ca molar proportion less than 0.25 which is either orthopyroxene (typically around 0.05 Ca) or pigeonite (typically around 0.10–0.15 Ca). Mg Con and Fe Con are better variables for the regression modeling than Mg# [Mg/(Mg + Fe)] because they account better for the effects of different proportions of Ca in the two pyroxene phases. We

derive a single multivariate linear regression equation to model Mg Con in both low-Ca and high-Ca pyroxene compositions despite the discontinuous nature of the relationship by introducing an indicator (or dummy) variable (DV; see Appendix 2.3.1). Example results are shown in Fig. 6a and b, and the regression equations for Mg Con are:
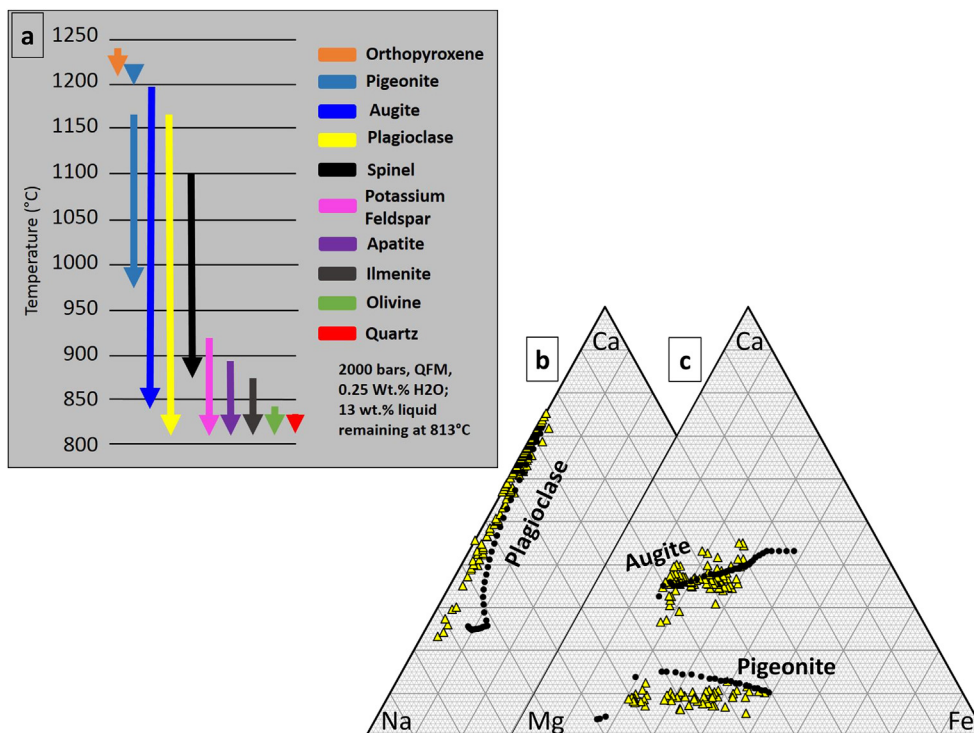
For sample EQ-169:

$$Mg \ (mol. \ \%) = 0.87608 - (0.00159 \times GS) + (0.000413 \times GS \times DV) - (0.27689 \times DV) \quad (4)$$

For sample DQ-136:

$$Mg \ (mol. \ \%) = 0.86805 - (0.00244 \times GS) - (0.16066 \times DV) \quad (5)$$

2.3.2. Evaluating significance, assumptions, and reliability

Table 2 provides data to evaluate the significance and fit of models for

Fig. 12. Results from the selected MELTS model. See Appendix section 3.3 and text for details. a) Sequence of minerals predicted to crystallize as a function of temperature. b) Plagioclase compositions in DQ-136 by EDS analysis (yellow triangles) compared with compositions predicted by MELTS (black filled circles). c) Pyroxene compositions in DQ-136 by EDS analysis (yellow triangles) compared with values predicted by MELTS (black filled circles). (For interpretation of the references to colour in this figure legend, the reader is referred to the web version of this article.)

Table 5

a) Mineral proportions in DQ-136 compared with MELTS model at last temperature step (813 °C). b) Mineral proportions in DQ-136 after crystallization of sub-ophitic and granular clusters compared with MELTS model (at temperature 1073 °C).

Mineral	Comp.[a]	Density[b]	Mode[c]	PCM[d]	MELTS[e]
	(mol %)	(g/cm[c])	(vol.%)	(wt.%)	(wt.%)
a)					
High-Ca pyroxene	Mg# = 64	3.32	23	30	33
Low-Ca Pyroxene	Mg# = 64.5	3.27	16	20	17
Plagioclase	An62	2.71	43	41	39
K-feldspar		2.6	4	3	4
Opaque minerals		4.77	4	6	7
b)					
High-Ca pyroxene	Mg# = 69.5	3.30	16	19	23
Low-Ca Pyroxene	Mg# = 66.5	3.27	14	16	17
Plagioclase	An66	2.71	28.5	27.5	24
Liquid		2.54	41.5	37.5	36

Notes

See text and Appendix section 3.3 for details of calculations.

[a] Weighted average of measured compositions.

[b] Linear approximation from end-members; MELTS data for opaque minerals and Liquid.

[c] Values from point count and pixel areas.

[d] Mode values converted to weight percent and normalized to 100%.

[e] MELTS values normalized to 100%.

samples EQ-169 and DQ-136. The p-value for the F-test shows that the models are significant in all cases. The R^2 value is the ratio of the variance explained by the model to total variance and shows how effectively the linear regression fits the data. The lower R^2 value for pyroxene in sample EQ-169 compared with sample DQ-136 (Table 2), despite the excellent visual fit to the data (Fig. 6), probably results from the more limited range of gray scale values and compositions in sample EQ-169. Plagioclase in sample DQ-136 does have a wide range of gray scale values and compositions but there are a few strong outliers in the dataset which probably account for the lower R^2 value (Table 2). The outliers could be due to errors in point compositions or operator-assigned gray scale values, but don't significantly affect the regression coefficients for fitting the overall trend. The assumptions of independence, homogeneity, and normality of residuals were evaluated using standard statistical procedures (Kleinbaum et al., 2014, p. 454–457). We employed cross-validation to test reliability by using the model regression equation to predict gray scale values from compositions in the holdout dataset. In cross-validation, a model is considered reliable if the shrinkage (defined as R^2 of model – R^2 of holdouts) is less than 0.10. Shrinkage values in Table 2 range from 0.001 to 0.01 which suggests that our models are reliable. The value of −0.17 for pyroxenes in sample EQ-169 suggests that the R^2 value for the pyroxenes model may actually be underestimated. An alternative suggestion is that the holdout population may be different from that used to build the model, but the randomly-selected holdout analyses are not skewed or significantly different from the rest.

2.4. PCM creation

2.4.1. Image separation based on mineral identification

In this stage, pixels in the primary BSE image that correspond to specific minerals or mineral compositions are digitally separated to create new images. If there are holes in the thin section, the corresponding black pixels can be separated first as described in Step 1 below. Image separation is straightforward for minerals that have unique gray scale values or value ranges on the primary BSE image. EDS element maps are essential for separating minerals with overlapping gray scale values. Pixels may need to be selected and removed in a particular sequence depending on overlapping gray-scale values or compositions. We describe our strategies for sample BoQ-3 in the following steps and in Fig. 7. This complex sample is representative of most of the expected challenges so the number of steps and operator time required (Fig. 2) are

Mg-rich cores in pigeonite: *dark orange*
b
c
d
Key for false colors:
Plagioclase: *yellow*
Augite: dark *blue*
Pigeonite: *light blue*
Quartz: *red*
Opaque minerals: *black and gray*
K-feldspar, biotite, hornblende: *pink*
a
up
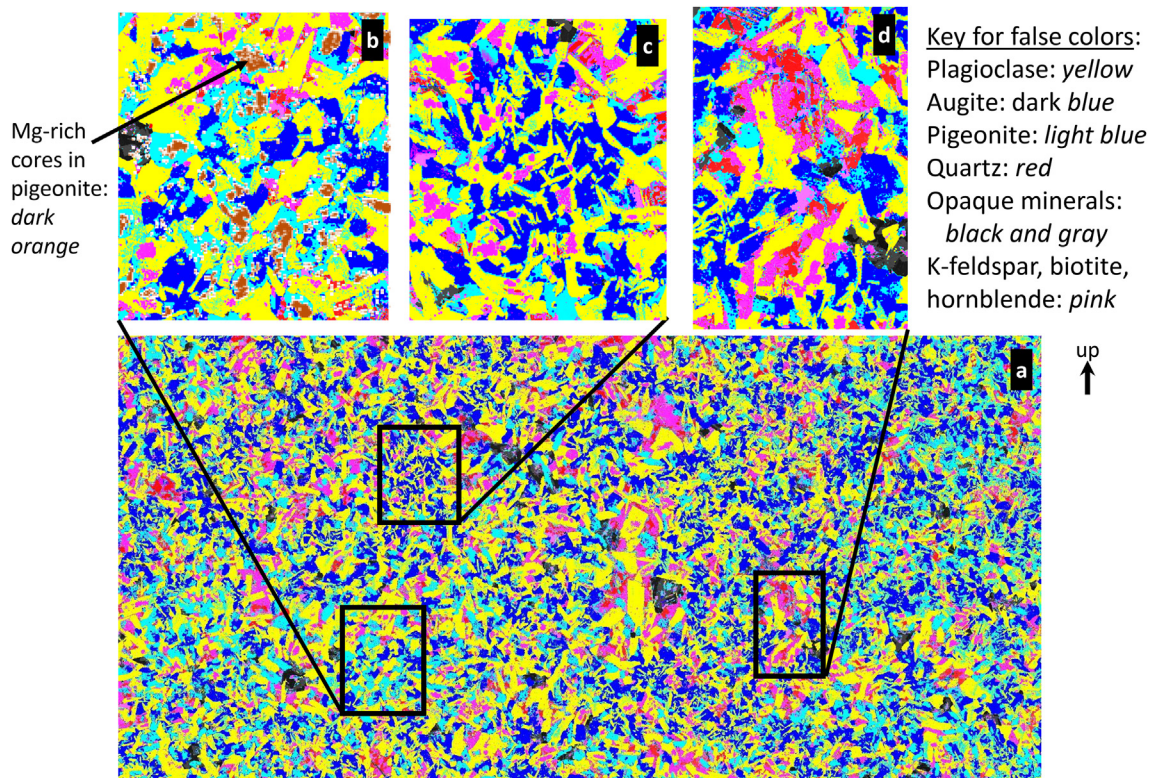
Fig. 13. PCM for all minerals in DQ-136. a) thin section area is 37.08 mm × 17.94 mm, contains 10582 × 5120 pixels, and has resolution of about 3.5 μm/pixel or 81 447 pixels/mm2. b) cropped and enlarged domain of granular texture with discrete grains of augite, pigeonite, and plagioclase. Note Mg-rich cores in pigeonite (dark orange color, arrow). c) cropped and enlarged domain of sub-ophitic texture with augite partly enclosing smaller plagioclase. d) cropped and enlarged domain of more abundant late-stage minerals: quartz, K-feldspar, biotite, hornblende.
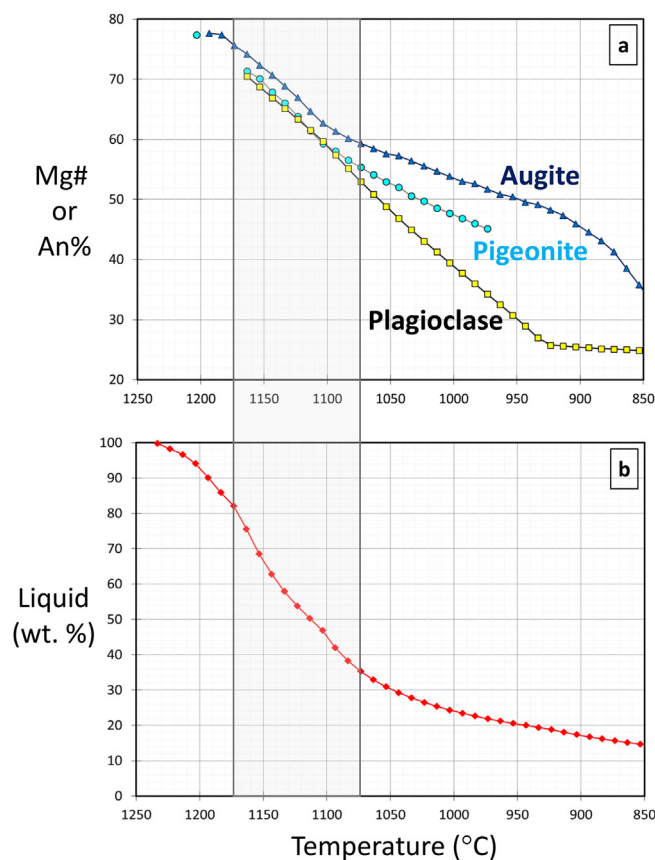
Fig. 14. Results from the selected MELTS model. Shaded region denotes the mineral compositions and temperature interval for crystallization of the sub-ophitic and granular clusters. See text for discussion. a) Predicted composition of augite (dark blue triangles), pigeonite (teal circles), and plagioclase (yellow squares) at each temperature step. Mg# is Mg/(Mg + Fe) in mol %; An is Ca/(Ca + Na) in mol %. b) Predicted weight percent liquid (red diamonds) remaining at each temperature step. (For interpretation of the references to colour in this figure legend, the reader is referred to the web version of this article.)

maximum estimates. We refer to actions in Adobe Photoshop but other comparable image processing software could be used instead.

Step 1: On the primary BSE image of sample BoQ-3, holes in the thin section have gray scale values of 0–2 and quartz has the next lowest gray scale values, while olivine and accessory minerals (oxides, sulfides, apatite, etc.) have unique gray scale values at the upper end of the range. For each of these minerals in turn, we selected pixels from the corresponding gray scale range using the color select tool in Photoshop, then cut and pasted them into a separate image (Fig. 7b–d). This process of selecting pixels within a gray scale range and cutting them out of images is also called thresholding in other image processing software. Fig. 7e is the BSE image with orange pixels representing the removed quartz, olivine, and accessory minerals.

Step 2: We used the potassium element map to identify pixels that correspond with potassium feldspar, biotite, and secondary muscovite that overlap with plagioclase feldspar. The potassium element map and alignment BSE were put in a separate layer and aligned with the BSE image after Step 1 processing (Fig. 7e). We selected the potassium-rich pixels, then switched to the processed BSE image layer and cut and pasted these pixels into a separate image (Fig. 7f). The resulting image with K-bearing phases removed is Fig. 7g.

Step 3: The pixels of plagioclase feldspar have a unique gray-scale range in the BSE image after Step 2 processing. These pixels were selected, cut and pasted in the same way as in Step 1 to create a separate image of plagioclase (Fig. 7h). The resulting image with plagioclase removed is Fig. 7i.

Step 4: The aluminum element map distinguishes minerals with gray

scale values that overlap with pyroxenes such as amphiboles, chlorite, and secondary alteration products. The selection, cutting, and pasting process is the same as in Step 2 to create a new image showing these Al-bearing minerals (Fig. 7j). This step had to be done after plagioclase and K-feldspar were separated because feldspars contain considerable aluminum. The resulting image after the removal of Al-bearing minerals is Fig. 7k.

Step 5: The pixels remaining in the BSE image (Fig. 7k) represent pyroxenes. The multicomponent solid solution of pyroxene means that a range of pyroxene compositions share the same gray scale value (Fig. 8). The shading in Fig. 8 mimics gray scale variation which depends almost entirely on Mg—Fe proportions and is almost independent of Ca proportion. Thus, gray-scale values alone cannot distinguish low-Ca pyroxene from high-Ca pyroxene. We employ a calcium element map to separate the two types of pyroxene following the same procedures as in steps 2 and 4. The result is low-calcium pyroxene in one image (Fig. 7l) and high-calcium pyroxene in another (Fig. 7m). None of our samples contained more than two pyroxenes in significant proportions.

Step 6: Multivariate linear regression models for minerals with solid solution enable the creation of PCMs for specific mineral composition ranges using Lookup Tables to assign false colors or threshold functions in software such as ImageJ (Rasband, 1997–2016), as shown in Fig. 1. Several additional examples are provided in the Results section below.

3. Results and discussion

The sizes, shapes, orientations, and distributions of crystals are critically important textural data for the interpretation of rock formation (e.g., Jerram and Davidson, 2007). Because the scale of a PCM can be adjusted continuously over three orders of magnitude without loss of resolution (entire thin section down to tens of micrometers) all parts of the sample are equally available for study and the integrity of phase identity, composition, and texture is preserved. A PCM can be adapted to many different methods of quantifying mineral compositions and textures. For example, estimates of mineral proportions based on pixel areas in a PCM correspond well, typically within 1–2%, with estimates made by standard point counting on a grid using a polarizing light microscope (Table 3). The PCM can be used to distinguish minerals with similar optical properties, such as pyroxenes. In this section we present brief examples using PCMs to investigate the crystallization of igneous rocks:

1) *the formation of mineral layering*: using a PCM to image centimeter-scale spatial patterns in mineral compositions to better constrain models of sidewall crystallization;
2) *grain size patterns and crystal growth*: using a PCM as the base image to measure different growth zones within crystals and evaluate changes in growth rates and processes;
3) *modeling stages of crystallization*: using mineral compositions predicted by thermodynamic modeling to threshold a PCM and show the spatial distribution of co-crystallizing minerals and interstitial liquid, "snapshots" of the magma during crystallization.

The full development of these applications is beyond the scope of this paper. The purpose of this section is to provide enough information to show that PCMs are a versatile petrologic tool and worth the time investment.

3.1. Application 1: compositional patterns in large-area images

The greater utility of large-area PCMs compared with small-area X-ray maps is illustrated by the PCM for plagioclase in sample DQ-6 (Fig. 9), the same diabase sample shown in Figs. 1 and 3. Sample DQ-6 was collected about 82 m from the northeast side contact or about one-third the distance across the 255-m wide Birdsboro dike, and contains alternating finer-grained, plagioclase-rich layers and coarser-grained, pyroxene-rich layers that parallel the nearly vertical dike contacts (see Fig. 3a).
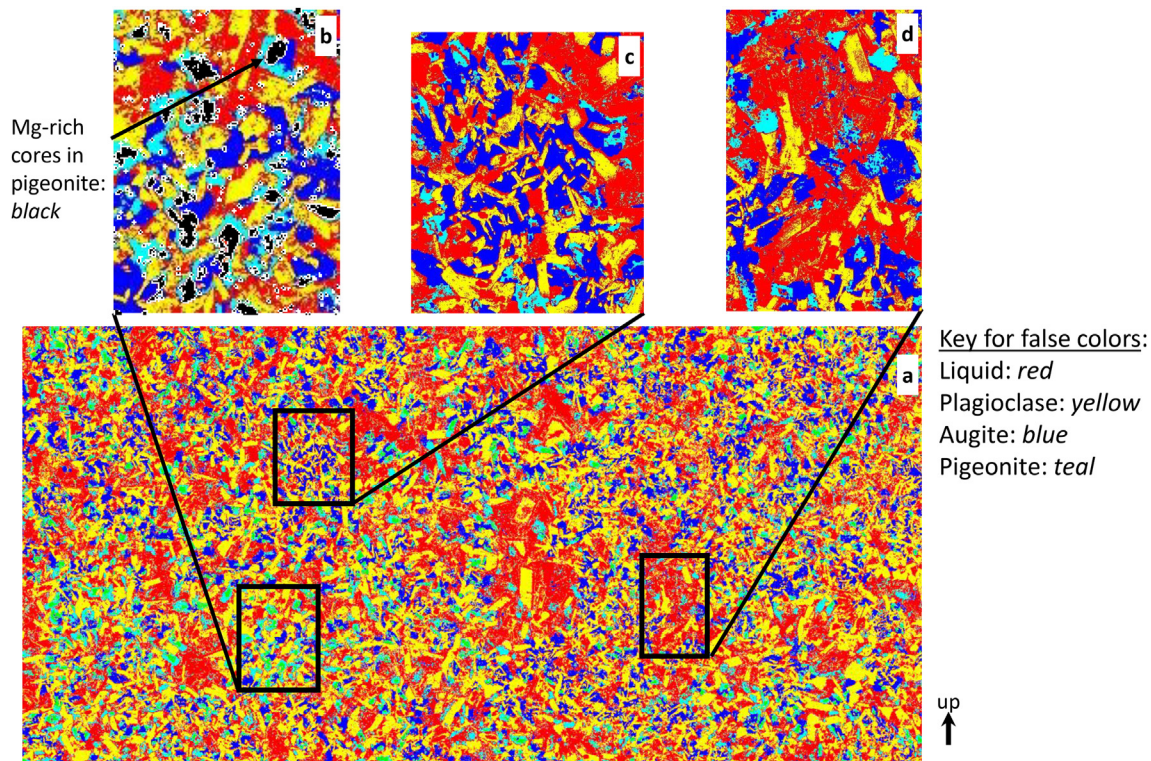
Fig. 15. PCM for DQ-136 at the end of the crystallization of sub-ophitic and granular clusters; < 3 wt.% spinel predicted by the MELTS model is not shown. a) thin section area, pixel resolution, and the areas outlined in black boxes are the same as in Fig. 13. b) cropped and enlarged granular cluster; Mg-rich pigeonite in black. c) cropped and enlarged subophitic cluster. d) cropped and enlarged domain of late-stage minerals. Distribution and abundance of residual liquid (red) should be noted.
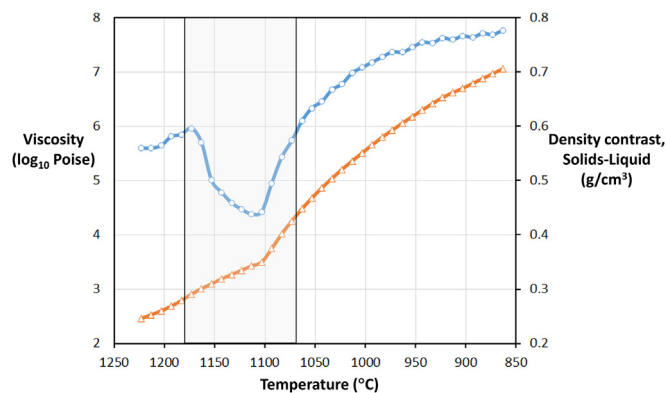

Fig. 16. The viscosity of the liquid (triangles and orange line) predicted by MELTS for each temperature step. The density contrast (circles and blue line) is the difference between the weighted density of the cumulative solid assemblage and the density of the liquid predicted by MELTS at each temperature step. The shaded region corresponds with the temperature interval for the crystallization of the sub-ophitic and granular clusters (same as in Fig. 14). (For interpretation of the references to colour in this figure legend, the reader is referred to the web version of this article.)

The plagioclase PCM (Fig. 9a–e) revealed an important spatial pattern in *composition* that we had not recognized despite polarizing light microscopy, BSE imaging, and over 200 EDS mineral analyses from four "representative" – but spatially isolated – layers. We had previously documented the micrometer-scale pattern inside individual plagioclase crystals that can be seen best in Fig. 9e: concentric shells that are more Ca-rich in the core and progressively more Na-rich to the rim (normal zoning). However, we had not seen the centimeter-scale variation in plagioclase composition across different layers in the section (Fig. 9a–e). The most Ca-rich plagioclase (red) is most abundant in the layer that is farthest from the dike sidewall contact (left side of each image in Fig. 9),

and the most Na-rich plagioclase (purple) is most abundant in the layer closest to the sidewall contact (right side of each image), the opposite of the trend expected for normal sidewall crystallization that progresses inward from the contact. A combined PCM for late-crystallizing quartz and K-bearing minerals (Fig. 9f) reveals variations in abundance in different modal layers, as well. This example illustrates how the greater range of length scales available in a PCM image makes it more likely to recognize significant compositional and textural variations than small-area X-ray maps or routine micro-analytical methods.

The patterns of plagioclase composition and late-stage phases cannot be explained solely by competing rates of thermal and chemical diffusion during sidewall crystallization, the commonly-proposed cause of modal layering in dikes (e.g., Parsons and Brown, 1988). The entire modally-layered section of the Birdsboro dike is a few to several meters wide, roughly 1000 times the dimension of modal layers in DQ-6 (Fig. 9). Any thermal or compositional gradient in the magma would not be steep enough to produce the observed range of plagioclase core composition from An_{60} to An_{39} over less than 40 mm (Fig. 9a–e). Moreover, there is no comparable variation in pyroxene core compositions in the different layers (Fig. 1a). This opens the possibility that the most Ca-rich plagioclase was brought in and sorted by pulses of replenishing magma. The variation in the abundance of late-crystallizing, lower-temperature quartz and K-feldspar across modal layers (Fig. 9f) suggests that residual liquid was able to migrate and was excluded from or concentrated within different modal layers during crystallization. The relatively large amount of late-crystallizing minerals in the same fine-grained layer with the most Ca-rich plagioclase – a high-temperature phase that crystallized near the liquidus – seems to contradict phase equilibria. Thus, the spatial distributions of different phases and mineral compositions observed in PCMs are critical evidence that multiple processes beyond diffusion rates are involved in sidewall crystallization. PCMs would be equally useful in studying other types of modal layering which, despite over a hundred years of investigation, remain controversial (e.g., Marsh, 2013, 2015; Latypov et al., 2015).
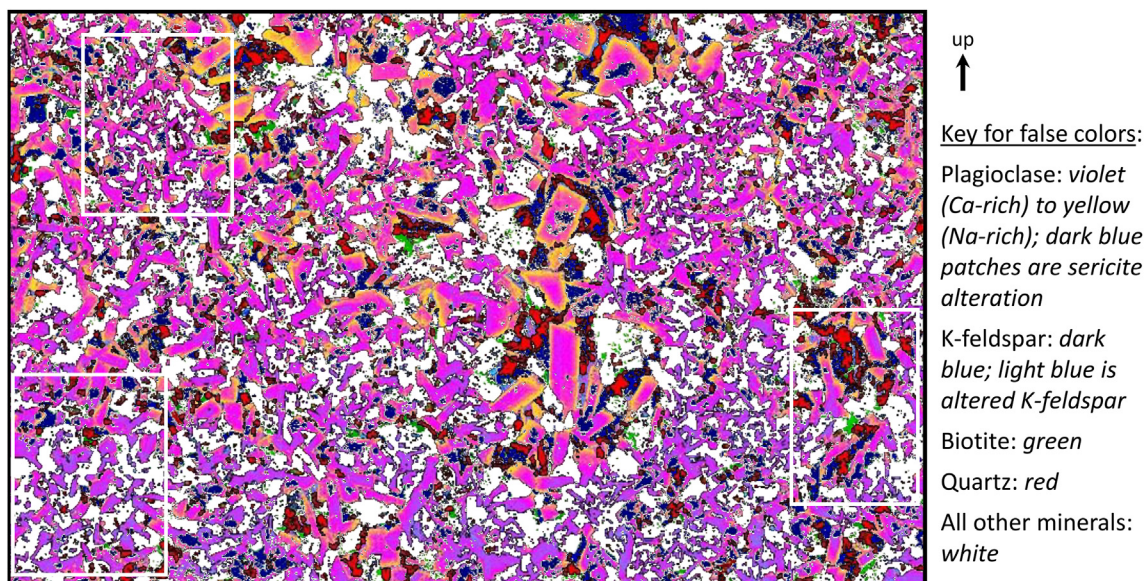
Fig. 17. PCM for sample DQ-136 highlighting late stage minerals. Cropped and enlarged central portion of the thin section; pixel resolution and areas within outlined boxes (white) are the same as in Fig. 13a and 15a. False colors were applied in ImageJ; the 6-shades LUT was used for plagioclase and the 5 ramps LUT for K-bearing minerals. The "speckling" consists of very small grains of quartz and K-feldspar, small patches of alteration (sericite), plagioclase inclusions in pyroxene, and biotite intergrown with oxide minerals. Distribution of Na-rich plagioclase, K-feldspar, quartz, and biotite should be noted.

3.2. Application 2: crystal size distributions of zoned crystals

Crystal size distributions (CSDs) have been used to evaluate the rates and processes of mineral growth since the 1980's (e.g., Marsh, 1988; Cashman and Marsh, 1988). CSDs are based on population density which requires that every grain in an area be measured, and the interpretation of CSDs depends on kinetic growth models. Recently, Riker and Cashman (2016) questioned the interpretation of CSDs based on the outer shapes of crystals in volcanic rocks and proposed incorporating experimental constraints and using alternative approaches to quantify crystal sizes and textures (see also Zieg, 2014). Our second application highlights three advantages of using a PCM to measure crystal sizes and shapes: 1) the PCM shows the entire thin section area and good resolution is maintained when smaller areas are enlarged for viewing; 2) the PCM can show just the mineral of interest without ambiguity in optical properties, overlapping gray scale values, or touching grains of different minerals; and 3) thresholds can be applied for minerals with solid solution so that portions of grains with different compositions can be imaged and measured separately. We conducted a feasibility study using a PCM of complexly-zoned plagioclase crystals to generate crystal size distributions (CSDs) for different growth zones (Figs. 10 and 11). Specific details of the procedures are in Appendix section 3.2.

Plagioclase in the selected sample (EQ-169) shows the three distinct compositional zones typically observed in the deep portions of the sills in our study area. Small cores are more Na-rich (An_{76-60}) and show normal zoning; there is a reversal to a Ca-rich shell (An_{81-76}) that commonly has oscillatory zoning; and the outer shell shows continuous normal zoning to rims with the most Na-rich composition (An_{76-44}). By applying composition thresholds in ImageJ to the plagioclase PCM we first verified the composition range for each shell across the entire thin section. Then we applied thresholds to the PCM in ImageJ to color the Ca-rich shells (An_{81-76}) in red and the cores and outer shells (An_{75-44}) in black (Fig. 10a); this served as the base image for manually outlining the individual shells within crystals in a small part of the thin section. The sizes and shapes of the cores, Ca-rich shells, and outer shells (entire grains) can be seen in the enlarged images of Fig. 10b–c; plagioclase grains contain one, two, or three shells depending on when they grew from the magma and the position of the section plane through the crystal. The PCM (Fig. 10a) made it easy to outline the cores and Ca-rich shells. The PCM

eliminated touching grains of other minerals but not touching grains of plagioclase, so the time required to outline the outer shells (entire grains) was reduced but still considerable. Image processing and grain measurements were made using ImageJ, and CSD calculations were done in Excel following the method in Zieg and Marsh (2012, p. 2572), (see Appendix section 3.2 for details).

For this feasibility study we did not measure enough grains in large enough areas to provide statistically representative samples (e.g., Higgins, 2006; Gualda, 2006). Even so, the preliminary results show that each compositional shell has a different CSD shape and slope (Fig. 11) that cannot be explained by sequential crystallization under the same conditions (Marsh, 1998; Higgins, 2006). For example, the CSD for the outer shells (entire grains) looks linear and similar to CSDs from the Peneplain Sill, Antarctica, (Marsh,1998), while the CSDs for the Na-rich cores and Ca-rich shells have steeper slopes. With additional measurements, the differences in slope and curvature for the different compositional shells could be evaluated more rigorously in terms of growth processes consistent with the compositional reversal and oscillatory zoning (e.g., Marsh, 1998; Higgins, 2006; Ustunisik et al., 2014; Perugini et al., 2005; Ginibre et al., 2002; 2007; Humphreys et al., 2006; Vernon, 2004).

This feasibility study demonstrates that a PCM image with composition thresholds can be used to measure different parts of zoned crystals and generate meaningful results such as CSDs. This method could be extended using the PCM and outline images to measure the spatial distributions (Jerram et al., 1996; 2003) or crystallographic orientations (e.g., Prior et al., 1999) of crystal populations with different compositions. PCMs that image textures and compositions of multiple crystal populations would also complement CSD and other studies of complexly-mixed magma chambers (e.g., Riker and Cashman, 2016; Bergantz et al., 2015; Cooper and Kent, 2014; Davidson et al., 2007; Marsh, 1998).

3.3. Application 3: combining PCMs with thermodynamic phase equilibria

The final application combines PCMs with thermodynamic models from the MELTS software package (Ghiorso and Sack, 1995; Asimow and Ghiorso, 1998) to investigate the sequential development of rock texture during in-situ crystallization. The MELTS algorithms are powerful tools

for forward modeling the sequence of phases and compositions from phase equilibria. Without MELTS, there is only textural evidence for the sequence of co-crystallizing minerals, and textures may be ambiguous (e.g., Vernon, 2004; Means and Park, 1994) or modified by later processes (e.g., Boudreau, 2011; McBirney, 2009). MELTS, however, does not predict rock texture. A PCM can show the spatial distribution of co-crystallizing minerals as predicted by MELTS, thereby integrating spatial and compositional information with a thermodynamic foundation. Reconstructing the entire crystallization history of a sample is a much larger study than can be included here and is the subject of a separate manuscript in preparation. Instead, we present two stages of crystallization and explore the development of touching crystal frameworks and the distribution and composition of trapped late-stage liquid. Touching frameworks of plagioclase crystals or plagioclase-augite intergrowths have been imaged previously in two and three dimensions (Philpotts and Carroll, 1996; Philpotts and Dickson, 2000, 2002; Philpotts et al., 1999; Jerram et al., 2010). Both natural samples and numerical models have provided insights into the rheology, porosity, and permeability of crystal mush but with limited or no compositional information (e.g., Jerram et al., 2003; 2010; Hersum and Marsh, 2007; Cheadle et al., 2004). PCMs combined with MELTS modeling integrate spatial distributions, mineral compositions, and rheological properties.

To be amenable to MELTS modeling, a rock sample should be close to a liquid composition and have a relatively simple crystallization history so that the mineral sequence and compositions track the evolving liquid composition. These criteria are met for sample DQ-136, a fine-grained diabase collected about 4 m from one sidewall contact of the Birdsboro Dike. This sample has no larger phenocrysts or modal layering and limited hydrothermal alteration. The bulk composition of DQ-136 is quite similar to the estimated average bulk liquid composition represented by two lava flows and four intrusion chill margins for major and trace elements (Table 4); chemical analysis methods are in Appendix section 3.3. Plagioclase and pyroxenes in DQ-136 have simple compositional zoning without reversals or indications of mixed crystal populations, consistent with an apparently simple crystallization history.

We made thirty runs of the MELTS software to obtain a forward model of fractional crystallization at temperature steps of 10 °C using sample DQ-136 as the starting liquid (Table 4) while varying pressure, oxygen fugacity, and water content (Appendix section 3.3). Results presented here are from the one model most consistent with the mineral modes and compositions in DQ-136. The sequence of mineral phases is shown graphically in Fig. 12a and the MELTS mineral proportions compare well with the actual mode (Table 5a). A few percent of orthopyroxene predicted as the first crystallizing phase in the MELTS model is probably present as the small, altered, mafic grains in the thin section. Plagioclase, augite, and pigeonite in DQ-136 all have compositions similar to the ranges predicted by MELTS (Fig. 12b and c). Differences in pyroxene compositions (Fig. 12c) probably result from some subsolidus exsolution and recrystallization.

Having established that DQ-136 is an appropriate sample for MELTS modeling, and having found a MELTS model that is a suitable fit to the sample mode and mineral compositions, we now turn to investigating the rock texture. Previous studies of correlative or similar mafic magmas (Palisades sill, Srogi et al., 2010; Holyoke basalt, Philpotts and Dickson, 2002) identified intergrowths of augite and plagioclase with ophitic to sub-ophitic texture as important crystal frameworks. However, our MELTS model predicts co-crystallization of plagioclase with both augite and pigeonite (Fig. 12a). The PCM of sample DQ-136 (Fig. 13) shows two distinct textural domains containing either pigeonite, augite, and plagioclase as discrete, granular grains (hereafter called granular clusters, Fig. 13b); or augite and plagioclase with sub-ophitic texture (sub-ophitic clusters, Fig. 13c). We used the regression models for pyroxenes and plagioclase and applied threshold functions in ImageJ to the PCMs to identify the range of compositions within the two types of crystal clusters. Augite and pigeonite show normal zoning (increase in iron toward the rims) and the same range of compositions in both cluster types:

$Mg\# = 78$–61 in augite and $Mg\# = 77$–55 in pigeonite. These compositions match those predicted by the MELTS model for crystallization down to 1073 °C, with the core compositions corresponding to growth before plagioclase joins the crystallizing assemblage (e.g., Mg-rich pigeonite cores shown in Fig. 13b). Plagioclase also has normal zoning (more Na-rich rims) and the same compositional range in both cluster types from An_{74} to An_{54}. This is very close to the plagioclase composition (An_{71} to An_{54}) predicted by the MELTS model to co-crystallize with the augite and pigeonite compositions from about 1173 °C to 1073 °C (Fig. 14a). The difference in the most calcic plagioclase compositions (An_{74} vs. An_{71}) is probably within the combined uncertainties of the EDS analyses, the regression model, and the MELTS model. Mineral proportions comprising the sub-ophitic and granular clusters and the proportion of residual liquid on the PCM are very similar to those predicted from the MELTS model (Table 5b), also indicating good correspondence between sample DQ-136 and the selected MELTS model. The touching framework in DQ-136 was more heterogeneous than those described in previous studies and consisted of sub-ophitic clusters of augite and plagioclase and granular clusters of pigeonite, augite, and plagioclase. The different textures did not result from different stages of crystallization, but must reflect intrinsic differences in nucleation and growth of adjacent phases.

A PCM for minerals that correspond with the MELTS model from the liquidus to 1073 °C was constructed by applying the composition thresholds in ImageJ (Fig. 15) and clearly shows touching frameworks of sub-ophitic and granular clusters surrounded by residual liquid (red pixels). The texture appears quite similar to images of numerical crystallization models such as Hersum and Marsh (2007, their Fig. 4). The touching framework of pyroxene-plagioclase clusters crystallized during important rheological transitions from a crystal suspension with 85% liquid to a crystal mush and then to a rigid crust with about 36% percent liquid (Fig. 14b). The touching framework with 36% interstitial liquid would have had relatively high permeability of 10^{-9} to 10^{-10} m^2 and pathways available for melt migration, according to work by Cheadle et al. (2004). However, touching frameworks with as much as 45–65% liquid have high compressive strength (Philpotts and Carroll, 1996) and resist mechanical compaction that otherwise drives melt migration (Marsh, 1996, 2002; Vigneresse et al., 1996; Hersum, 2009; Špillar and Dolejš, 2015). Thus, melt migration would have depended on the relative buoyancy and viscosity of the residual liquid – factors that can be estimated from MELTS model data. The crystallization interval of the clusters comprising the touching framework corresponds with significant changes in liquid viscosity and the relative density of the crystals and liquid (Fig. 16). The density difference drops sharply by about 25% between 1173 °C and 1103 °C (Fig. 16) as the liquid becomes more Fe-rich, reducing buoyancy forces that would impel the liquid to migrate. Below 1103 °C as Fe—Ti oxide (ulvöspinel) crystallizes, the liquid viscosity increases more steeply (Fig. 16), which would also limit the ability of the melt to move. The sub-ophitic and granular clusters thus crystallized in the interval when falling density contrast and rising viscosity reduced buoyancy and restricted circulation of the liquid through the crystal mush. The integration of spatial and composition data from the PCM with thermodynamic forward models and estimated magma properties from MELTS leads us to a better understanding of how a simple solidification zone crystallized and why residual liquid was trapped instead of migrating out of the developing crystal framework.

We also use PCMs to visualize the distribution of late-stage minerals that crystallized from the residual liquid in DQ-136. The PCM in Fig. 15 shows some interstitial liquid in the granular and sub-ophitic clusters (Fig. 15b and c), but most liquid is concentrated in pockets (Fig. 15d) presumably due to progressive exclusion of the liquid as the touching framework developed. The PCM of the final rock (Fig. 13) shows that the melt pockets become domains with more abundant late-stage phases such as potassium feldspar, quartz, granophyre, and biotite (compare Figs. 15d and 13d). By applying a composition threshold to the

plagioclase PCM in ImageJ, we can incorporate Na-rich plagioclase into a PCM showing all late-stage phases (Fig. 17), and measure pixel areas to estimate that the most Na-rich plagioclase (An$_{20-25}$) makes up about 2.5% of the rock mode. Fig. 17 shows that quartz and K-feldspar occur as separate interstitial grains within the granular and sub-ophitic clusters, but are more intergrown as granophyre in domains with more of the late-stage minerals. The textural difference suggests that residual liquids had different compositions or crystallized differently depending on location within a heterogeneous crystal mush. The roles of trapped liquid and reactive transport during the final stages of magma crystallization remain contentious questions in petrology (e.g., Boudreau, 2011; McBirney, 2009; Meurer and Meurer, 2006; Steefel et al., 2005). The characterization of the abundance, composition, and distribution of late-stage minerals is a critical first step in addressing these questions, and a PCM can provide all of this information in a single image (e.g., Fig. 17).

3.4. Conclusions

Phase Composition Maps show the spatial arrangements of minerals and mineral compositions at scales ranging from tens of millimeters (a standard rock thin section) to tens of micrometers without loss of resolution. The PCM method takes advantage of the ability to collect high resolution BSE images more rapidly and over larger areas than standard X-ray mapping. BSE gray scale values are calibrated with EDS mineral analyses, and multivariate linear regression models are applied for minerals with solid solution. The regression models are used to threshold images of gray scale value by composition to create PCMs for one or more minerals or mineral composition ranges. The method described in this paper produces PCMs with image resolution as good as a WDS X-ray map, but showing mineral phases and compositions rather than elemental concentrations. The new QEMSCAN technology may produce similar images, but PCMs can be made with widely-available SEM-EDS instrumentation. Because PCMs integrate compositional, spatial, and textural information they can be used to connect actual rocks with models of rock formation.

Acknowledgements

Appendix A. Supplementary data

Supplementary data related to this article can be found at http://dx.doi.org/10.1016/j.cageo.2017.08.009.

References

Asimow, P.D., Ghiorso, M.S., 1998. Algorithmic modifications extending MELTS to calculate subsolidus phase relations. Am. Mineral. 83, 1127–1131.

Bergantz, G.W., Schleicher, J.M., Burgisser, A., 2015. Open-system dynamics and mixing in magma mushes. Nat. Geosci. 8, 793–796. http://dx.doi.org/10.1038/ngeo2534.

Boudreau, A., 2011. The evolution of texture and layering in layered intrusions. Int. Geol. Rev. 53, 330–353.

Cashman, K.V., Marsh, B.D., 1988. Crystal size distribution (CSD) in rocks and the kinetics and dynamics of crystallization II: Makaopuhi Lava Lake. Contrib. Mineral. Petrol. 99, 292–305.

Cheadle, M.J., Elliott, M.T., McKenzie, D., 2004. Percolation threshold and permeability of crystallizing igneous rocks: the importance of textural equilibrium: Geology 32, 757–760. http://dx.doi.org/10.1130/G20495.1.

Cooper, K.M., Kent, A.J.R., 2014. Rapid remobilization of magmatic crystals kept in cold storage. Nature 506, 480–483.

Davidson, J.P., Morgan, D.J., Charlier, B.L.A., Harlou, R., Hora, J.M., 2007. Microsampling and isotopic analysis of igneous rocks: implications for the study of magmatic systems. Annu. Rev. Earth Planet. Sci. 35, 273–311.

Ghiorso, M.S., Sack, R.O., 1995. Chemical mass transfer in magmatic processes. IV. A revised and internally consistent thermodynamic model for the interpolation and extrapolation of liquid-solid equilibria in magmatic systems at elevated temperature and pressures. Contrib. Mineral. Petrol. 119, 197–212.

Ginibre, C., Kronz, A., Worner, G., 2002. High-resolution quantitative imaging of plagioclase composition using accumulated backscattered electron images: new constraints on oscillatory zoning. Contrib. Mineral. Petrol. 142, 436–448. http://dx.doi.org/10.1007/s004100100298.

Ginibre, C., Worner, G., Kronz, A., 2007. Crystal zoning as an archive for magma evolution. Elements 3, 261–266.

Gottlieb, P., Wilkie, G., Sutherland, D., Ho-tun, E., Suthers, S., Perera, K., Jenkins, B., Spencer, S., Butcher, A., Rayner, J., 2000. Using quantitative electron microscopy for process mineralogy applications. JOM J. Miner. Met. Mater. Soc. 52, 24–25. http://dx.doi.org/10.1007/s11837-000-0126-9.

Gualda, G.A.R., 2006. Crystal size distributions derived from 3D datasets: sample size versus uncertainties. J. Pet. 47, 1245–1254.

Hames, W.E., McHone, J.G., Renne, P.R., Ruppel, C. (Eds.), 2003. The Central Atlantic Magmatic Province: Insights from fragments of Pangea: Washington, D.C. Geophysical Monograph, vol 136. American Geophysical Union, 267 pp.

Hersum, T., 2009. Consequences of crystal shape and fabric on anisotropic permeability in magmatic mush. Contrib. Mineral. Petrol. 157, 285–300. http://dx.doi.org/10.1007/s00410-008-0334-9.

Hersum, T.G., Marsh, B.D., 2007. Igneous textures: on the kinetics behind the words. Elements 3, 247–252.

Higgins, M.D., 2006. Quantitative Textural Measurements in Igneous and Metamorphic Petrology. Cambridge University Press, Cambridge, U.K, 265 pp.

Humphreys, M.C.S., 2009. Chemical evolution of intercumulus liquid, as recorded in plagioclase overgrowth rims from the Skaergaard Intrusion. J. Petrol. 50, 127–145. http://dx.doi.org/10.1093/petrology/egn076.

Humphreys, M.C.S., Blundy, J.D., Sparks, R.S.J., 2006. Magma evolution and open-system processes at Shiveluch Volcano: insights from phenocryst zoning. J. Petrol. 47, 2303–2334. http://dx.doi.org/10.1093/petrology/eg1045.

Jerram, D.A., Cheadle, M.J., Hunter, R.H., Elliott, M.T., 1996. The spatial distribution of grains and crystals in rocks. Contrib. Mineral. Pet. 125, 60–74.

Jerram, D.A., Cheadle, M.J., Philpotts, A.R., 2003. Quantifying the building blocks of igneous rocks: are clustered crystal frameworks the foundation? J. Pet. 44, 2033–2051. http://dx.doi.org/10.1093/petrology/egg069.

Jerram, D.A., Davidson, J.P., 2007. Frontiers in textural and microgeochemical analysis. Elements 3, 235–296.

Jerram, D.A., Davis, G.R., Mock, A., Charrier, A., Marsh, B., 2010. Quantifying 3D crystal populations, packing and layering in shallow intrusions: a case study from the Basement Sill, Dry Valleys, Antarctica. Geosphere 6, 537–548. http://dx.doi.org/10.1130/GES00538.1.

Ketcham, R.A., Carlson, W.D., 2001. Acquisition, optimization and interpretation of X-ray computed tomographic imagery: applications to the geosciences. Comput. Geosci. 27, 381–400. http://dx.doi.org/10.1016/s008-3004(00)00116-3.

Kleinbaum, G.D., Kupper, L.L., Nizam, A., Rosenberg, E.S., 2014. Applied Regression Analysis and Other Multivariable Methods, fifth ed. Cengage Learning, Boston, Massachusetts. 1051pp.

Latypov, R., Morse, T., Robins, B., Wilson, R., Cawthorn, G., Tegner, C., Holness, M., Lesher, C., Barnes, S., O'Driscoll, B., Veksler, I., Higgins, M., Wilson, A., Namur, O., Chistyakova, S., Naslund, R., Thy, P., 2015. A fundamental dispute: a discussion of "On some fundamentals of igneous petrology" by Bruce D. Marsh, Contributions to Mineralogy and Petrology (2013) 166: 665-690. Contrib. Mineral. Petrol. 169, 1–10. http://dx.doi.org/10.1007/s00410-015-1108-9.

Marsh, B.D., 1988. Crystal size distribution (CSD) in rocks and the kinetics and dynamics of crystallization I: Theory. Contrib. Mineral. Petrol. 99, 277–291.

Marsh, B.D., 1996. Solidification fronts and magmatic evolution. Mineral. Mag. 60, 5–40.

Marsh, B.D., 1998. On the interpretation of crystal size distributions in magmatic systems. J. Pet. 39, 553–599.

Marsh, B.D., 2002. On bimodal differentiation by solidification front instability in basaltic magmas, part 1: basic mechanics. Geochim. Cosmochim. Acta 66, 2211–2229.

Marsh, B.D., 2013. On some fundamentals of igneous petrology. Contrib. Mineral. Petrol. 166, 665–690. http://dx.doi.org/10.1007/s00410-013-0892-3.

Marsh, B.D., 2015. Reply: Contributions to Mineralogy and Petrology, vol. 169, pp. 1–9. http://dx.doi.org/10.1007/s00410-015-1110-2.

Martinson, P.J., Srogi, L., Willis, K.V., Lutz, T., Pollock, M., 2015. Geochemical, petrologic, and structural evidence for magmatic plumbing in the Morgantown Pluton and Jacksonwald Syncline, western Newark Basin, Central Atlantic Magmatic Province, USA. In: Geological Society of America Abstracts with Program, 47, p. 3.

Marzoli, A., Jourdan, F., Puffer, J.H., Cuppone, T., Tanner, L.H., Weems, R.E., Bertrand, H., Cirilli, S., Bellieni, G., De Min, A., 2011. Timing and duration of the Central Atlantic magmatic province in the Newark and Culpeper basins, eastern U.S.A. Lithos 122, 175–188.

McBirney, A.R., 2009. Factors governing the textural development of Skaergaard gabbros: a review. Lithos 111, 1–5. http://dx.doi.org/10.1016/j.lithos.2008.09.009.

Means, W.D., Park, Y., 1994. New experimental approach to understanding igneous texture. Geology 22, 323–326.

Meurer, W.P., Meurer, M.E.S., 2006. Using apatite to dispel the "trapped liquid" concept and to understand the loss of interstitial liquid by compaction in mafic cumulates: an example from the Stillwater Complex, Montana. Contrib. Mineral. Pet. 151, 187–201. http://dx.doi.org/10.1007/s00410-005-0054-3.

Parsons, I., Brown, W.L., 1988. Sidewall crystallization in the Klokken intrusion; zoned ternary feldspars and coexisting minerals. Contrib. Mineral. Pet. 98, 431–443.

Perugini, D., Poli, G., Valentini, L., 2005. Strange attractors in plagioclase oscillatory zoning: petrological implications. Contrib. Mineral. Pet. 149, 482–497. http://dx.doi.org/10.1007/s00410-005-0667-6.

Philpotts, A.R., Brustman, C.M., Shi, J., Carlson, W.D., Denison, C., 1999. Plagioclase-chain networks in slowly cooled basaltic magma. Am. Mineral. 84, 11–12.

Philpotts, A.R., Carroll, M., 1996. Physical properties of partly melted tholeiitic basalt. Geology 24, 1029–1032.

Philpotts, A.R., Dickson, L.D., 2000. The formation of plagioclase chains during convective transfer in basaltic magma. Nature 406, 59–61. http://dx.doi.org/10.1038/35017542.

Philpotts, A.R., Dickson, L.D., 2002. Millimeter-scale modal layering and the nature of the upper solidification zone in thick flood-basalt flows and other sheets of magma. J. Struct. Geol. 24, 1171–1177.

Pret, D., Sammartino, S., Beaufort, D., Meunier, A., Fialin, M., Michot, L.G., 2010. A new method for quantitative petrography based on image processing of chemical element maps: Part I. Mineral mapping applied to compacted bentonites. Am. Mineral. 95, 1379–1388. http://dx.doi.org/10.2138/am.2010.3431.

Prior, D.J., Boyle, A.P., Brenker, F., Cheadle, M.C., Day, A., Lopez, G., Peruzzo, L., Potts, G.J., Reddy, S., Spiess, R., Timms, N.E., Trimby, P., Wheeler, J., Zetterström, 1999. The application of electron backscatter diffraction and orientation contrast imaging in the SEM to textural problems in rocks. Am. Mineral. 84, 1741–1759.

Rasband, W.S., 1997-2016. ImageJ. U. S. National Institutes of Health, Bethesda, Maryland, USA. http://imagej.nih.gov/ij/.

Riker, J., Cashman, K.V., 2016. Interpreting pyroclast textures: re-evaluating crystal size distributions in the context of new views of magmatic systems. EOS Trans. Am. Geophys. Union 2016.

Rudge, J.F., Holness, M.B., Smith, G.C., 2008. Quantitative textural analysis of packings of elongate crystals. Contrib. Mineral. Petrol. 156, 413–429. http://dx.doi.org/10.1007/s00410-008-0293-1.

SAS, May, 2016. Knowledge base documentation v. 9.4. http://support.sas.com/documentation/.

Špillar, V., Dolejš, D., 2014. Kinetic model of nucleation and growth in silicate melts: implications for igneous textures and their quantitative descriptions. Geochim. Cosmochim. Acta 131, 164–183. http://dx.doi.org/10.1016/j.gca.2014.01.022.

Špillar, V., Dolejš, D., 2015. Melt extraction from crystal mushes: numerical model of texture evolution and calibration of crystallinity-ordering relationships. Lithos 239, 19–32. http://dx.doi.org/10.1016/j.lithos.2015.10.001.

Srogi, L., Lutz, T., Dickson, L., Pollock, M., Gimson, K., Lynde, N., 2010. Magmatic layering and intrusive plumbing in the Jurassic Morgantown Sheet, Central Atlantic Magmatic Province. In: Fleeger, G.M., Whitmeyer, S.J. (Eds.), The Mid-Atlantic Shore to the Appalachian Highlands, Geological Society of America Field Guide, vol. 16, pp. 51–68.

Steefel, C.I., DePaolo, D.J., Lichtner, P.C., 2005. Reactive transport modeling: an essential tool and a new research approach for the Earth sciences. Earth Planet. Sci. Lett. 240, 539–558. http://dx.doi.org/10.1016/j.epsl.2005.09.

Togami, S., Takano, M., Kumazawa, M., 2000. An algorithm for the transformation of XRF images into mineral-distribution maps. Can. Mineral. 38, 1283–1294.

Ustunisik, G., Kilinc, A., Nielsen, R.L., 2014. New insights into the processes controlling compositional zoning in plagioclase. Lithos 200-201, 80–93.

Vernon, R.H., 2004. A Practical Guide to Rock Microstructure. Cambridge University Press, Cambridge, 594 pp.

Vigneresse, J.L., Barbey, P., Cuney, M., 1996. Rheological transitions during partial melting and crystallization with application to felsic magma segregation and transfer. J. Petrol. 37, 1579–1600.

Withjack, M.O., Schlische, R.W., Malinconico, M.L., Olsen, P.E., 2012. Rift-basin development; lessons from the Triassic-Jurassic Newark Basin of eastern North America. In: Geological Society Special Publications, 369, pp. 301–321.

Zieg, M.J., Marsh, B.D., 2012. Multiple reinjections and crystal-mush compaction in the Beacon sill, McMurdo Dry Valleys, Antarctica. J Pet. 53, 2567–2591.

Zieg, M.J., 2014. Petrologic evolution of a Nipigon diabase sill, Ontario, Canada: insights from compositional and textural profiles. Econ. Geol. 109, 1383–1401.